

A Search for Massive Galaxy Population in a Protocluster of LAEs at $z = 2.39$ near the Radio Galaxy 53W002

NAOKI YONEKURA,¹ MASARU KAJISAWA,^{1,2} ERIKA HAMAGUCHI,¹ KEN MAWATARI,³ AND TORU YAMADA⁴

¹Graduate School of Science and Engineering, Ehime University, 2-5 Bunkyo-cho, Matsuyama, Ehime 790-8577, Japan

²Research Center for Space and Cosmic Evolution, Ehime University, 2-5 Bunkyo-cho, Matsuyama, Ehime 790-8577, Japan

³National Astronomical Observatory of Japan, 2-21-1 Osawa, Mitaka, Tokyo 181-8588, Japan

⁴Institute of Space and Aeronautical Science, Japanese Aerospace Exploration Agency, 3-1-1, Yoshinodai, Chuo-ku, Sagami-hara, Kanagawa, 252-5210, Japan

ABSTRACT

We searched massive galaxy population in the known large-scale high-density structure of Lyman α emitters (LAEs) at $z = 2.39$ near the radio galaxy 53W002 by using B , V , i' , J , H , and K_s -bands imaging data taken with Suprime-Cam and MOIRCS on the Subaru telescope. We selected 62 protocluster member candidates by their JHK_s -band colors and photometric redshift analysis (JHK_s -selected galaxies) in our survey field of 70.2 arcmin², and compared their physical properties estimated from the SED fitting with a comparison sample in the COSMOS field. We found significant number density excesses for the JHK_s -selected galaxies in the 53W002 field at $K_s < 22.25$, $J - K_s > 2$, or $V - K_s > 4$. In particular the number density of the JHK_s -selected galaxies with $K_s < 22.25$ and $J - K_s > 2$ in the 53W002 field is eight times higher than the comparison sample. Most of those with $K_s < 22.25$ and $J - K_s > 2$ are massive galaxies with $M_s > 10^{11} M_\odot$, and their sSFRs of 10^{-11} – 10^{-10} yr⁻¹ suggest that the star formation has not yet stopped completely. We also found a density excess of quiescent galaxies with $M_s = 5 \times 10^{10}$ – $10^{11} M_\odot$ and sSFR $< 10^{-11}$ yr⁻¹ as well as that of low-mass galaxies with $M_s = 10^{9.75}$ – $10^{10} M_\odot$ and various sSFRs. The massive galaxies with $M_s > 10^{11} M_\odot$ are not located at the density peaks of LAEs, but they show a wide distribution along the similar direction with the structure of LAEs over ~ 15 – 20 comoving Mpc. On the other hand, the quiescent galaxies with sSFR $< 10^{-11}$ yr⁻¹ clearly avoid the structure of LAEs. Our results suggest that massive galaxies also exist in this protocluster discovered by the moderate overdensity of LAEs and their star formation activity depends on location in the protocluster.

Keywords: galaxies: clusters: individual — galaxy: formation — evolution — high-redshift

1. INTRODUCTION

In the present universe, galaxy clusters are dominated by massive early-type galaxies, while there are many spiral galaxies in field environments (e.g., Dressler 1980; Goto et al. 2003). Those early-type galaxies in clusters show similarly red optical colors and form the color-magnitude relation or red sequence in the color-magnitude plain (e.g., Bower et al. 1992). Such red sequences of massive cluster members have been discovered at progressively higher redshifts up to $z \sim 2$ (e.g., Aragon-Salamanca et al. 1993; Stanford et al. 1998; Sny-

der et al. 2012; Willis et al. 2020). The tightness of their red colors suggests that stars in these massive cluster galaxies were formed at $z > 2$ (Bower et al. 1992). In the Λ CDM paradigm of structure formation, it is predicted that such clusters have been formed hierarchically from smaller halos, and their progenitors, namely protoclusters, consist of hundreds of halos and extend over tens of comoving Mpc at $z > 2$ (e.g., Chiang et al. 2013; Muldrew et al. 2015). Therefore, direct observations of protoclusters at $z > 2$ are important to understand the formation and evolution of massive cluster galaxies.

Targeting high-redshift radio galaxies is an efficient way to find protoclusters. These galaxies tend to be the most massive galaxies with $M_s > 10^{11} M_\odot$ in the early universe (e.g., Seymour et al. 2007), which suggests

that they can be good markers of high-density peaks, and actually reside in high-density environments more frequently than normal (non-AGN) similarly massive galaxies (Hatch et al. 2014). Many narrow-band imaging observations searching for line emitters around radio galaxies have successfully discovered protoclusters at $z > 2$ (e.g., Le Fevre et al. 1996; Pascarelle et al. 1996b; Kurk et al. 2000; Pentericci et al. 2000; Venemans et al. 2002, 2004, 2005, 2007; Kuiper et al. 2011; Hayashi et al. 2012; Cooke et al. 2014; Husband et al. 2016). The overdensities of Lyman break galaxies (LBGs) around the radio galaxies have been found by the broad-band color selection technique (e.g., Miley et al. 2004; Overzier et al. 2006, 2008). The similar near-infrared (NIR) color-selection methods for Balmer break galaxies were used to search high-density regions of massive galaxies in the radio galaxy fields (Kajisawa et al. 2006; Hatch et al. 2011a).

Wide-field surveys with the narrow-band imaging and/or the broad-band color selection technique mentioned above have also discovered high-redshift protoclusters which are not biased to the radio galaxy fields (e.g., Steidel et al. 1998, 2000, 2005; Shimasaku et al. 2003; Ouchi et al. 2005; Geach et al. 2012; Toshikawa et al. 2012, 2016, 2018; Lee et al. 2014; Lemaux et al. 2014; Diener et al. 2015; Bădescu et al. 2017; Jiang et al. 2018; Higuchi et al. 2019). The Lyman break technique with wide-field optical imaging can search a large volume effectively, but the spectroscopic confirmation is essential to avoid the chance alignment effect. The line emitter searches with narrow-band imaging have the advantage of selecting galaxies at the same redshift, while their survey volume tends to be limited. The wide-field optical narrow-band observations searching for Lyman α emitters (LAEs) can both mitigate the limited survey volume and keep effectiveness of picking up high-density regions of galaxies at the same redshift.

On the other hand, LAEs typically have a low stellar mass of $\sim 10^9 M_{\odot}$ and young stellar age of several tens of Myr (e.g., Gawiser et al. 2007). LBGs and other line emitters such as $H\alpha$ and [OIII] are basically star-forming galaxies. Therefore these selection methods could miss massive galaxies and/or quiescent ones with little star formation, which are similar with massive early-type galaxies dominated in the present clusters. Since the rest-frame optical–NIR SEDs give us the information of old stellar population of galaxies, the NIR follow-up observations for protoclusters are important to understand the formation and growth of massive galaxies in the high-density environments. In particular, such follow-up observations are essential to confirm whether massive galaxies have already formed or not in

the high-density structures of LAEs, which tends to be very young and less dusty low-mass galaxies.

However, the number of such NIR follow-up studies for protoclusters is still limited. Uchimoto et al. (2012) and Kubo et al. (2013) found that NIR-selected massive galaxies show a significant number excess along the large-scale structure of LAEs in the SSA22 field, which is one of the largest protoclusters discovered so far (Yamada et al. 2012). Kubo et al. (2015, 2021) spectroscopically confirmed that many of the massive galaxies are protocluster members. Shi et al. (2019a) also found a significant excess of NIR-selected Balmer break galaxies in a rich structure of LAEs and LBGs at $z = 3.78$ (Lee et al. 2014; Dey et al. 2016). Furthermore, several studies reported a segregation in the spatial distribution between LAEs and more massive galaxies in protoclusters (e.g., Shimakawa et al. 2017b; Shi et al. 2019a, 2020). It is unclear whether massive galaxies exist or not and how they distribute if exist in other or more moderate and typical protoclusters of LAEs.

In this study, we use optical and NIR imaging data taken with Suprime-Cam and MOIRCS on the Subaru telescope to search massive galaxies in a large-scale high-density structure of LAEs at $z = 2.39$ discovered by Mawatari et al. (2012) near the radio galaxy 53W002. The 53W002 protocluster was initially discovered as an overdensity of 18 LAEs selected by the intermediate-band excess of HST/WFPC2 data around the radio galaxy (Pascarelle et al. 1996a,b). Keel et al. (1999) carried out a wider ground-based imaging observation over $14'3 \times 14'3$ area with a similar intermediate-band filter and found 14 LAE candidates. Yamada et al. (2001) performed a NIR imaging observation in the WFPC2 field. They found that the LAEs are very faint or not detected in the NIR data and there are few massive quiescent galaxy candidates at the redshift with bright NIR magnitudes and red colors. Mawatari et al. (2012) observed $31' \times 24'$ field with Suprime-Cam and a custom-made narrow-band filter for the Ly α emission at $z \sim 2.39$. They discovered a large-scale high-density structure of LAEs in north or northeast of 53W002, and found that the radio galaxy is located at outskirts of the structures. The overdensity of LAEs in this structure is not as extremely high as the SSA22 protocluster, and corresponds to a moderately rich structure. We search massive galaxies over a ~ 70 arcmin² field along the structure of LAEs with the optical–NIR imaging data, and compare their statistical properties with similarly selected field galaxies in the COSMOS field.

This paper is organized as follows: We describe observations and data reduction in Section 2. The procedures of selecting candidates for protocluster members

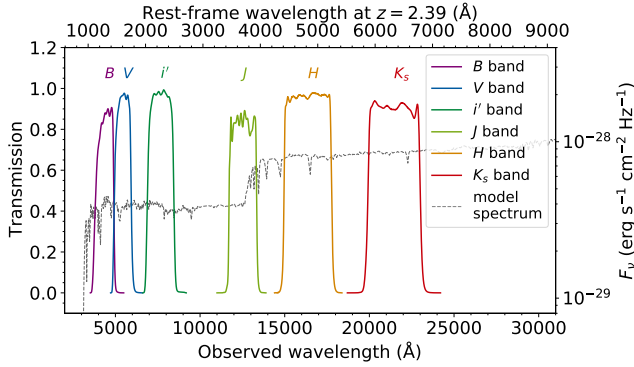


Figure 1. Transmission curves of filters used in this study and a model spectrum at $z = 2.39$. The color solid lines show the transmission curves of the filters. Grey dashed line shows the model spectrum at $z = 2.39$ from [Bruzual & Charlot \(2003\)](#) with age of 1 Gyr and star-formation history of $\text{SFR} \propto \exp(-t/1 \text{ Gyr})$.

at $z = 2.39$ and estimating their physical properties are described in Section 3. We present results in Section 4 and discuss them in Section 5. The summary is given in Section 6. We use the AB magnitude system ([Oke & Gunn 1983](#)). We assume cosmological parameters of $H_0 = 70 \text{ km s}^{-1} \text{ Mpc}^{-1}$, $\Omega_m = 0.3$, and $\Omega_\Lambda = 0.7$.

2. OBSERVATIONS & DATA REDUCTION

2.1. Data and Reduction

In this study, we used the B , V , i' , J , H , and K_s -band imaging data. Figure 1 shows the transmission curves of them and a model spectrum of a galaxy at $z = 2.39$. The wavelengths of B , V , and i' bands correspond to the ultraviolet in the rest frame at $z = 2.39$. Those of J , H , and K_s bands correspond to the optical in the rest frame, and the Balmer/4000Å break falls between the J and H bands at $z = 2.39$. The summary of observations is given in Table 1.

The B , V , and i' -band images were observed by Subaru Prime Focus Camera (Suprime-Cam: [Miyazaki et al. 2002](#)) mounted on the 8.2 m Subaru telescope. Figure 2 shows the fields of view of the observations and the spatial distribution and number density map of LAEs discovered by [Mawatari et al. \(2012\)](#). The blue solid line indicates the field of view of the optical observations, and they cover the large-scale structure of LAEs. The B -band image was provided by [Mawatari et al. \(2012\)](#). The V and i' -band observations were done on 2015 April 15 and 2016 May 16 with the same field of view (centered at RA=17:14:15.2, Dec=+50:15:15.2) as the B -band image. The weather condition on 2015 April 15 was cloudy, and only i' -band imaging with 30 min on-source exposure was done under $0''.80$ - $1''.4$ seeing. On 2016 May 16, we took both V and i' -band data through thin clouds

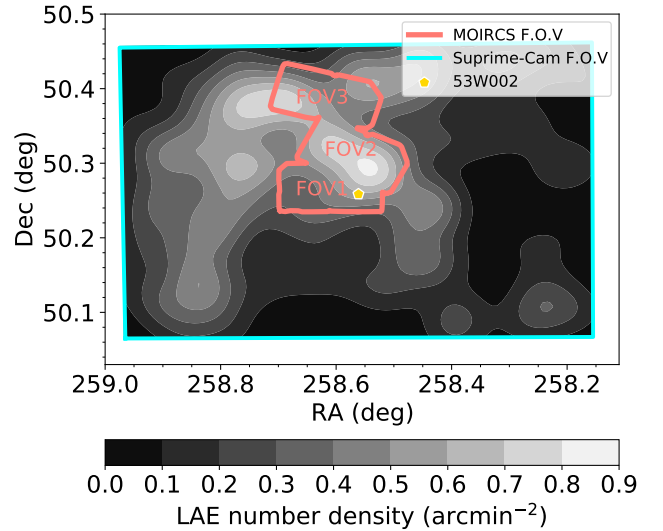


Figure 2. Fields of view of Suprime-Cam and MOIRCS observations. The blue solid line shows the Suprime-Cam field of view, while the red solid line shows the MOIRCS field of view. The grey contour shows the LAE number density smoothed with a Gaussian kernel with $\sigma = 1.5$ from [Mawatari et al. \(2012\)](#).

under $0''.6$ - $1''.2$ seeing. The data reduction for the V and i' -band images was done by using SDFRED version 2.0 ([Yagi et al. 2002](#); [Ouchi et al. 2004](#)). Several frames with low S/N due to the bad condition were excluded before combining images. The final exposure time for the V and i' -band images are 1.3 and 1.5 hr, respectively. The PSF FWHMs of the reduced V and i' -band images are $0''.87$ and $1''.1$, respectively. These observations were the non-photometric conditions, and therefore the photometric calibration was done by comparing optical and NIR colors of stars in the observed data with those of Landolt standard stars ([Landolt 1992](#)).

The J , H , and K_s -band data were taken by Multi Objects InfraRed Camera and Spectrograph (MOIRCS: [Ichikawa et al. 2006](#); [Suzuki et al. 2008](#)) on the Subaru telescope. MOIRCS covers a field of view of $4' \times 7'$ by two HgCdTe HAWAII-2 detectors, namely chip-1 and chip-2, with a pixel scale of $0''.117 \text{ pixel}^{-1}$. As shown in Figure 2, we observed three fields of view of MOIRCS, namely, FOV1, FOV2, and FOV3. The FOV1 is the most southern one and contains the radio galaxy 53W002. The FOV2 covers 53W002F-HDR, a high-density region of LAEs at $z = 2.39$, discovered by [Mawatari et al. \(2012\)](#). The FOV3 is located in north of FOV2 and covers another high-density region of LAEs in the northeast. The FOV1 was observed on 2008 July 22-23 and 2007 April 27, while the FOV2 and FOV3 were observed on 2013 April 23-24 and 2014 June 13. The observations of the FOV1 were carried out in photometric and good-seeing

conditions and one of UKIRT Faint Standard stars, FS27 (Leggett et al. 2006) was also observed in the same nights for calibration. The other two fields were observed in non-photometric conditions under $0''.5$ - $0''.7$ seeing and no standard star was available for these data.

We reduced the J , H , and K_s -bands data with MCSRED (Tanaka et al. 2011). The reduction methods were basically the same as described in Kajisawa et al. (2011). In addition to basic procedures such as flat-fielding, median-sky subtraction, distortion correction, shift, and adding, the defringing process described in Kajisawa et al. (2011) was applied for the FOV1 data. The defringing process was not applied for the FOV2 and FOV3 data because “fringe-free” filters with wedged substrates were used in the observations of these two fields. Since no standard star was available for the FOV2 and FOV3 data, we estimated zero-point magnitudes for these two fields from those of the FOV1 field by matching fluxes of objects in the overlapping regions among the different fields. Then we additionally corrected zero-point offsets among the different bands in the same field by using the color tracks of Galactic stars.

Since we select our sample by JHK_s -band colors and then apply an additional criterion based on the optical-NIR SED fitting, we need to measure NIR or optical-NIR colors after correcting the difference of PSF size. The PSF FWHMs of the V and i' -bands data are larger than those of the NIR data (Table 1), and matching the PSF of the NIR data to the optical one leads to unnecessary loss of S/N ratio in the NIR color selection described in the next section. In order to avoid this problem, we made two kinds of images: one is the images whose PSFs are matched among only the NIR data, and the other is those whose PSFs are matched to the worst one (i' band). First, we matched PSF among the J , H , and K_s -band images to measure the NIR colors for the color selection. By using IRAF/PSFMATCH, all NIR images were matched to PSF FWHM of $0''.77$, which corresponds to that of the H -band image of the FOV2 chip-1 data smoothed with a Gaussian kernel with $\sigma = 1.5$ pixel. Second, we matched PSF FWHM among the B , V , i' , J , H , and K_s -band images for the SED fitting. We converted the B , V , and i' -band images to the same image size and pixel scale of the K_s -band one by using the IRAF/GEOTRAN. After that, all images were matched to PSF FWHM of $1''.2$, which corresponds to that of the i' -band image smoothed with a Gaussian kernel.

The limiting magnitudes of the final combined and PSF-matched data for each field and chip are summarized in Table 2.

2.2. Source Detection and Photometry

We carried out the source detection in the K_s -band images by using the software SExtractor version 2.5.0 (Bertin & Arnouts 1996). A detection threshold of 1.2-times the local background root mean square over 15 connected pixels was used. We used a region where the exposure time was more than half of maximum value in the JHK_s -band images to keep homogenous depth in each field, and the exposure maps were used for WIGHT_MAP of SExtractor. The Kron magnitude from SExtractor was used as the total K_s -band magnitude of detected objects. We used objects with $K_s < 23.3$, which was the brightest 5σ limiting magnitude in the MOIRCS fields. Finally, we detected 2381 objects in the area of 70.2 arcmin^2 . In order to measure colors, we performed aperture photometry with $1''.6$ and $2''.0$ diameter apertures on the images with PSF matched among the JHK_s and $BVi'JHK_s$ bands by using dual image mode of SExtractor, respectively.

In order to estimate the background noise, we made sky images by masking object pixels in the data with pseudo noise images, which was made from the sky region of the original images. We then measured fluxes at many random positions in the sky images with the same $1''.6$ and $2''.0$ diameter apertures as the object photometry, and used their standard deviation as the background error.

3. ANALYSIS

3.1. Sample Selection

We basically selected member galaxy candidates in the 53W002 protocluster at $z \sim 2.39$ by a color-selection method with JHK_s bands proposed by Kajisawa et al. (2006). This color selection is defined by the Vega system, and can be expressed in the AB system¹ as follows:

$$\begin{aligned} (J - K_s)_{\text{AB}} &> 0.581 \\ &\text{and} \\ (J - K_s)_{\text{AB}} &> 2(H - K_s)_{\text{AB}} + 0.541. \end{aligned} \tag{1}$$

This selection is based on the fact that the Balmer/4000Å break falls between the J and H bands at $2 \lesssim z \lesssim 3$. With this selection, we can pick up not only passively evolving galaxies but also star-forming galaxies at $z \sim 2.5$ except for very young ones without

¹ Conversions between the Vega and AB system in the J , H , and K_s bands of MOIRCS are $J_{\text{AB}} = J_{\text{Vega}} + 0.915$, $H_{\text{AB}} = H_{\text{Vega}} + 1.354$, and $K_{s \text{ AB}} = K_{s \text{ Vega}} + 1.834$, respectively.

Table 1. Summary of observed data used in this paper.

Band	Instrument	Field	Date	Exposure-time (hr)	PSF FWHM ^a (")	Reference
<i>B</i>	Suprime-Cam/Subaru		2009 May 22-23	1.0	0.86	Mawatari et al. (2012)
<i>V</i>	Suprime-Cam/Subaru		2016 May 16	1.3	0.87	
<i>i'</i>	Suprime-Cam/Subaru		2015 April 15, 2016 May 16	1.5	1.1	
<i>J</i>	MOIRCS/Subaru	FOV1	2006 July 22-23, 2007 April 27	0.6	0.39/0.38	
		FOV2	2013 April 24-25, 2014 June 13	1.1	0.61/0.63	
		FOV3	2013 April 23-24, 2014 June 13	1.2	0.59/0.59	
<i>H</i>	MOIRCS/Subaru	FOV1	2006 July 22-23, 2007 April 27	0.7	0.45/0.42	
		FOV2	2013 April 24-25, 2014 June 13	1.1	0.63/0.59	
		FOV3	2013 April 23-24, 2014 June 13	1.0	0.49/0.49	
<i>K_s</i>	MOIRCS/Subaru	FOV1	2006 July 22-23, 2007 April 27	0.7	0.49/0.42	
		FOV2	2013 April 24-25, 2014 June 13	1.3	0.48/0.52	
		FOV3	2013 April 23-24, 2014 June 13	0.8	0.48/0.47	

^aIn the NIR data, PSF FWHM values for the two detectors of MOIRCS, namely, chip-1 (left part of the field of view) and chip-2 (right part) in each field are shown.

Table 2. Limiting magnitudes in each field.

Field	1'6 aperture ^a			2'0 aperture ^b					
	<i>J</i>	<i>H</i>	<i>K_s</i>	<i>B</i>	<i>V</i>	<i>i'</i>	<i>J</i>	<i>H</i>	<i>K_s</i>
FOV1 chip-1	23.9	23.6	23.5	28.3	27.6	26.8	24.9	24.6	24.5
chip-2	23.8	23.4	23.4	28.3	27.6	26.8	24.8	24.4	24.6
FOV2 chip-1	24.0	23.5	23.7	28.3	27.5	26.8	25.0	24.4	24.2
chip-2	23.8	23.3	23.4	28.3	27.6	26.8	24.7	24.2	24.4
FOV3 chip-1	23.9	23.4	23.3	28.3	27.6	26.8	24.9	24.3	24.3
chip-2	23.6	23.3	23.3	28.4	27.7	26.9	24.6	24.2	24.2

^a5 σ limiting magnitude.

^b2 σ limiting magnitude.

significant Balmer/4000Å break. The effect of dust extinction on this selection is small because the reddening vector is parallel to this criteria (Figure 2 in Kajisawa et al. 2006). In this selection, we removed objects with $S/N < 3$ in *H* band, because these objects have only lower limit of the $H - K_s$ color and could not necessarily satisfy the second criterion in equation (1). By using this color selection, we selected 80 objects with $K_s < 23.3$ in the 53W002 field. The radio galaxy 53W002 does not satisfy the JHK_s -color criteria due to the effect of very strong emission lines from AGN (Motohara et al. 2001). Kajisawa

et al. (2011) performed this color selection in the MOIRCS Deep Survey and confirmed that selected objects have a redshift distribution showing a strong peak at $z \sim 2.5$ with relatively small contamination. However our observations were shallower than that, so it is possible that foreground/background objects come into the sample due to the photometric error. Therefore, we set the additional criterion to reduce the contamination by applying the SED fitting to the optical and NIR photometry.

For the SED fitting, we used 2''0 aperture fluxes of the B , V , i' , J , H , and K_s bands. As the template spectra, we used the stellar population synthesis library of the GALAXEV (Bruzual & Charlot 2003). We assumed the initial mass function of Chabrier (2003) and three kinds of metallicities ($Z=0.004$, 0.008 , and 0.02). The assumed star-formation histories were exponentially declining SFR ($\text{SFR} \propto e^{-t/\tau}$, hereafter τ model), delayed- τ exponentially declining SFR ($\text{SFR} \propto t \times e^{-t/\tau}$, hereafter delayed τ model), single burst, and constant SFR. The timescale τ for the τ and delayed τ models ranges from 0.001 to 10 Gyr. The duration of star formation in the single burst model ranges from 0.01 to 1.8 Gyr. The range of age is between 50 Myr and the cosmic age at each redshift. The redshift range is between 0.01 and 4.99. We used the extinction law of Calzetti et al. (2000) with a range $E(B - V) = 0.0\text{--}2.0$. We also assumed the IGM absorption of Madau (1995). We note that the nebular emission is not included in the model templates. Strong nebular emission lines such as [OII] λ 3727, [OIII] λ 4959, 5007, $H\alpha$, and so on could significantly affect the SED of galaxies, in particular, for those with a very young age. With the COSMOS2015 catalog described in the next subsection, we found that including the nebular emission in the templates leads to catastrophic failure in the redshift estimation with our 6-band photometric SEDs for some (relatively small) fraction of sample galaxies, while excluding the nebular emission rarely causes such failure. Therefore we chose not to include the nebular emission in the model templates and checked the effects of the nebular emission on our results separately in Appendix A.

We used the minimum χ^2 method to obtain the best-fit model. The χ^2 was calculated as follows:

$$\chi^2 = \sum_{\text{filters } i} \frac{(A \times f_{i,\text{model}} - f_{i,\text{obs}})^2}{\sigma_i^2}, \quad (2)$$

where A , $f_{i,\text{model}}$, $f_{i,\text{obs}}$, and σ_i are a normalized factor, flux of model spectrum, observed flux, and error of observed flux, respectively. In order to take account of the variation of the IGM absorption among lines of sight (e.g., Thomas et al. 2017), we added the half value of $f_{i,\text{model}}$ to the σ_i in quadrature depending on the fraction of shorter wavelengths than 1216Å in the rest frame in each filter.

In order to remove the contamination from the JHK_s -band color-selected sample, we used the difference between the minimum χ^2 at the best-fit redshift and $z = 2.39$ (hereafter we call $\Delta\chi_{z=2.39}^2$). We defined the $\Delta\chi_{z=2.39}^2$ as follows:

$$\Delta\chi_{z=2.39}^2 \equiv \chi_{z=2.39}^2 - \chi_{\text{min}}^2, \quad (3)$$

where $\chi_{z=2.39}^2$ and χ_{min}^2 are the minimum values of χ^2 at $z = 2.39$ and the best-fit redshift, respectively. A higher value of $\Delta\chi_{z=2.39}^2$ means that the observed SEDs cannot be reproduced well by models at $z = 2.39$ and there is high probability of other redshifts. Therefore we adopted the criterion of the $\Delta\chi_{z=2.39}^2$ to exclude contamination as follows:

$$\Delta\chi_{z=2.39}^2 < 2.71. \quad (4)$$

This criterion means that 90% confidence interval of the best-fit redshift includes $z = 2.39$. Finally, we selected 62 objects by using the JHK_s -color cuts and the $\Delta\chi_{z=2.39}^2$ criterion in the 53W002 field (hereafter JHK_s -selected galaxies). In the next subsection, we demonstrate how the two-step selection works by using the multi-wavelength catalog from the COSMOS survey.

3.2. Comparison Sample

In order to measure a number density excess of the JHK_s -selected galaxies in the 53W002 field and compare statistical properties of them with field galaxies, we constructed a comparison sample with the same selection method in a general field from the COSMOS2015 catalog (Laigle et al. 2016). The COSMOS2015 catalog has multi-bands photometry from ultraviolet to far-infrared wavelength in a large area of about 2 deg², and also includes B , V , i' , J , H , and K_s bands, which are similar with those used in the 53W002 field. We note that the B , V , and i' -band data were taken by Suprime-Cam (Taniguchi et al. 2007), while these J , H , and K_s -band data were taken by VIRCAM mounted on VISTA telescope (McCracken et al. 2012). Objects in this catalog were detected on the combined $zYJHK_s$ -bands image. The redshift is estimated by using SED fitting with about 30 bands photometric data, including the broadband and medium-band filters from near-UV to mid-infrared. Laigle et al. (2016) compared their estimated photometric redshifts with spectroscopic redshifts and calculated the dispersion of $(z_{\text{photo}} - z_{\text{spec}})/(1 + z_{\text{spec}})$ (hereafter σ_z) and the fraction of catastrophic failure, namely, $|z_{\text{photo}} - z_{\text{spec}}|/(1 + z_{\text{spec}}) > 0.15$ (hereafter η). They reported that galaxies of zCOSMOS faint sample at $z = 1.5\text{--}2.5$ show $(\sigma_z, \eta) = (0.0032, 0.08)$, while those of 80 galaxies from MOSDEF survey (Kriek et al. 2015) are $(0.042, 0.10)$. Furthermore, several quiescent galaxies sample at $z \sim 1.2\text{--}2.5$ show low σ of 0.017–0.069 with no catastrophic failure (see Laigle et al. 2016 for more details).

In this study, we used the B , V , i' , J , H , and K_s -band fluxes measured with a 3'' diameter aperture. We selected objects with FLAG_COS=1 and FLAG_DEEP=1 to use objects in both the COSMOS field and UltraDeep

stripes of the UltraVISTA survey. It should be noted that objects in ultra-deep stripe 4, the most western one, were excluded because the area overlapped with the COSMOS field is too small to sample a random field of view of about $10' \times 10'$ (see Section 4.1). Since the different depth of the data could affect the sample selection, we performed Monte-Carlo simulations where random shifts were added to the J , H , and K_s -band fluxes of the COSMOS2015 catalog to match the flux errors with those of the 53W002 data as follows:

$$F = F_0 + R_{gauss} \times \sqrt{\sigma_{53W002}^2 - \sigma_{COSMOS}^2}, \quad (5)$$

where F , F_0 , R_{gauss} , σ_{53W002} , and σ_{COSMOS} are a simulated flux, original flux in the COSMOS2015 catalog, random numbers that follow a normal distribution with a mean of zero and a standard deviation of one, the median background error in the 53W002 field, and that in the COSMOS field, respectively. We note that the procedure mentioned above was not applied for the optical data, because the optical data in the 53W002 field have a same depth or slightly deeper than that in the COSMOS field. After convolving the NIR fluxes, we selected objects with the total K_s -band magnitude brighter than 23.3, which is the same limiting magnitude as in the 53W002 field. We corrected for the offset between the total and aperture magnitude by using the `OFFSET_MAG`, which was calculated by averaging the offsets in the optical to NIR bands with weight of the inverse square of the photometric error. Finally, we selected 36155 objects in 1230 arcmin².

We then selected galaxies at $z \sim 2.39$ with the same selection method as in the 53W002 field for the COSMOS2015 sample mentioned above (i.e., the JHK_s -color and $\Delta\chi_{z=2.39}^2$ selections). 1283 objects were selected by the JHK_s -color cuts. We note that objects with $H > 23.8$, which is the brightest 3σ limiting magnitude of the H band in the 53W002 field, were removed to match the selection method to that for the 53W002 sample. We then applied the $\Delta\chi_{z=2.39}^2$ criterion of the equation (4) and finally selected 976 galaxies. Figure 3 shows the distribution of the photometric redshift from the COSMOS2015 catalog for the selected objects. The red dashed and blue solid line histograms represent objects selected only with the JHK_s -color cuts (without the $\Delta\chi_{z=2.39}^2$ criterion) from the catalogs before and after the random flux shifting mentioned above. The comparison between these redshift distributions suggests that a larger photometric error leads to a larger fraction of contamination from other redshifts, especially from lower redshifts. The light blue shaded histogram in Figure 3 shows the final comparison sample. One can see

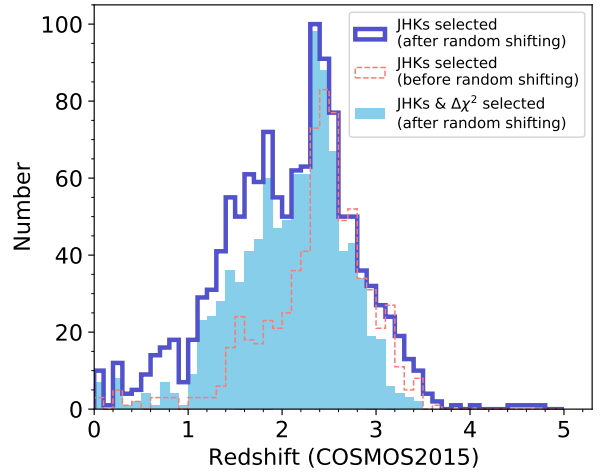


Figure 3. Redshift distribution of the selected sample in the COSMOS field. The photometric redshifts from the COSMOS2015 catalog (Laigle et al. 2016) are used. The blue open histogram shows the distribution for those selected by the JHK_s -bands color criteria after adding noises to fluxes in the catalog (see text), while the red dashed line represents those selected by the same color cuts with the original fluxes. The shaded histogram shows those selected by the JHK_s -bands color and $\Delta\chi_{z=2.39}^2$ criteria after adding the noises.

that the addition of the $\Delta\chi_{z=2.39}^2$ criterion mitigates the contamination caused by the larger flux errors.

3.3. Physical Properties

Assuming that the selected member candidates are at $z = 2.39$, we estimated physical properties such as stellar mass (M_s), star formation rate (SFR), dust extinction, and so on, of these galaxies from the results of the SED fitting described in Section 3.1. We corrected the stellar mass and star-formation rate for the offset between the total and aperture magnitudes. For this correction we used the difference between the aperture and total magnitudes in the K_s band for the 53W002 sample and `OFFSET_MAG` for the COSMOS sample as mentioned above. We calculated SFR averaged over the past 100 Myr from the best-fit star formation history (SFH) and use it in this study rather than the instantaneous SFR, which tends to have large uncertainty in our SED fitting setup (assumed parametric forms of SFH). The specific SFR (sSFR) was estimated by dividing the obtained star formation rate (averaged over the past 100 Myr) by the stellar mass. As an indicator of the stellar age, we used the mass-weighted age as follows:

$$\text{mass-weighted age} = \frac{\int_0^{\text{age}} (\text{age} - t) \times \text{SFR}(t) dt}{\int_0^{\text{age}} \text{SFR}(t) dt}, \quad (6)$$

where age and $SFR(t)$ are the age of the best-fit model spectrum and SFR as a function of time elapsed from the formation epoch (the beginning of star formation), respectively. We note that all stars formed since the formation epoch are included in the calculation.

4. RESULTS

4.1. Number Density Excess in the 53W002 Field

In this subsection, we compare the number density of the JHK_s -selected galaxies in the 53W002 field with that in the COSMOS field. By the JHK_s -color cuts and $\Delta\chi^2_{z=2.39}$ selection, we selected 62 objects with $K_s < 23.3$ in the 53W002 field over 70.2 arcmin^2 . On the other hand, 976 objects were selected in the COSMOS field over 1230 arcmin^2 . These results correspond to the number densities of 0.88 and 0.79 arcmin^{-2} , respectively. In order to estimate the field-to-field variation for the number density of the JHK_s -selected galaxies in an area of the 53W002 field, we performed a Monte-Carlo simulation with the COSMOS2015 catalog. We set $10' \times 10'$ fields of view at random positions in the COSMOS field, and calculated the number density in each field, which has a similar effective area with the 53W002 field after excluding masked regions. We repeated 100 such procedures. As a result, the median value and standard deviation of the number density in the random fields are 0.74 and 0.18 arcmin^{-2} , and 12% of the Monte-Carlo realizations in the COSMOS field show a higher number density than that in the 53W002 field.

The left panel of Figure 4 shows the K_s -band number counts of the JHK_s -selected galaxies in the 53W002 and COSMOS fields. The error bars show the 16 and 84 percentiles of the number density estimated from the same Monte-Carlo simulation in the COSMOS field. The number density of the JHK_s -selected galaxies with $K_s < 22.25$ in the 53W002 field is two times higher than that in the COSMOS field, and no random field of view in the simulation shows the number density higher than the 53W002 field. While there is a possible deficit in the $K_s = 22.25\text{--}22.5$ bin, a marginal excess can be seen at $K_s > 22.5$, where the number density in each bin is consistent with the COSMOS field within the uncertainty.

The middle and right panels of Figure 4 show the color distributions of the $J - K_s$ and $V - K_s$, respectively. There is a density excess of red objects with $J - K_s > 2$ in the 53W002 field. The fraction of random fields of view with a higher density of such red objects than that in the 53W002 field is 13%. In the right panel, red objects with $V - K_s > 4$ also show a density excess, and only 1% of the random field of view in the COSMOS field reproduces the number density in the 53W002 field.

We also focused on such red objects with $K_s < 22.25$, where the number density excess is seen in the number count. These bright and red objects with $K_s < 22.25$ and $J - K_s > 2$ ($V - K_s > 4$) in the 53W002 field show a number density about eight (three) times higher than those in the COSMOS field. None of random fields of view in the COSMOS field show a higher density of these bright and red objects than the 53W002 field. The number densities for these samples are summarized in Table 3.

We note that the JHK_s -selected galaxies with blue colors of $J - K_s < 1.5$ or $V - K_s < 3$ also show number density excess in the 53W002 field. 16 and 10% of the Monte-Carlo realizations in the COSMOS field show a higher number density than the 53W002 field for those with $J - K_s < 1.5$ and $V - K_s < 3$, respectively.

Figure 5 shows the color-magnitude diagrams in the 53W002 and COSMOS fields. The $J - K_s$ colors of these bright and red objects in the 53W002 field show a relatively large scatter rather than a tight ‘‘red sequence’’ found in lower-redshift clusters (Kodama et al. 2007).

4.2. Physical Properties

The left panel of Figure 6 shows the stellar mass distribution of the JHK_s -selected galaxies. The Red and blue lines indicate results in the 53W002 and COSMOS fields, respectively. The number density in the 53W002 field is higher than that in the COSMOS field at $M_s \gtrsim 10^{11} M_\odot$ and $M_s < 10^{10} M_\odot$. The middle and right panels of Figure 6 show the stellar mass distributions for the JHK_s -selected galaxies with $sSFR > 10^{-10} \text{ yr}^{-1}$ and $sSFR < 10^{-10} \text{ yr}^{-1}$, respectively. From these panels, one can see that those with $sSFR < 10^{-10} \text{ yr}^{-1}$ mainly contribute the number density excess in the 53W002 field. The number density of the JHK_s -selected galaxies with $sSFR < 10^{-10} \text{ yr}^{-1}$ is about 1.4 times higher than those in the COSMOS field, while that of those with $sSFR > 10^{-10} \text{ yr}^{-1}$ is about 0.8 times of the comparison sample. For the JHK_s -selected galaxies with $sSFR < 10^{-10} \text{ yr}^{-1}$ ($sSFR > 10^{-10} \text{ yr}^{-1}$), 3% (59%) of the Monte-Carlo realizations in the COSMOS field show a higher number density than that in the 53W002 field. In particular, the number density excess of those with $sSFR < 10^{-10} \text{ yr}^{-1}$ is significant at $M_s > 10^{10.75} M_\odot$ and $M_s = 10^{9.75}\text{--}10^{10} M_\odot$, where no Monte-Carlo realization shows a higher number density than that in the 53W002 field. On the other hand, galaxies with higher $sSFR$ show a density excess only at $M_s < 10^{10} M_\odot$, and a marginal deficit at $M_s > 10^{10} M_\odot$.

We also investigated the relation between $sSFR$ and M_s . Panels (a) and (b) of Figure 7 show $sSFR$ vs. M_s in the 53W002 and COSMOS fields. In the 53W002

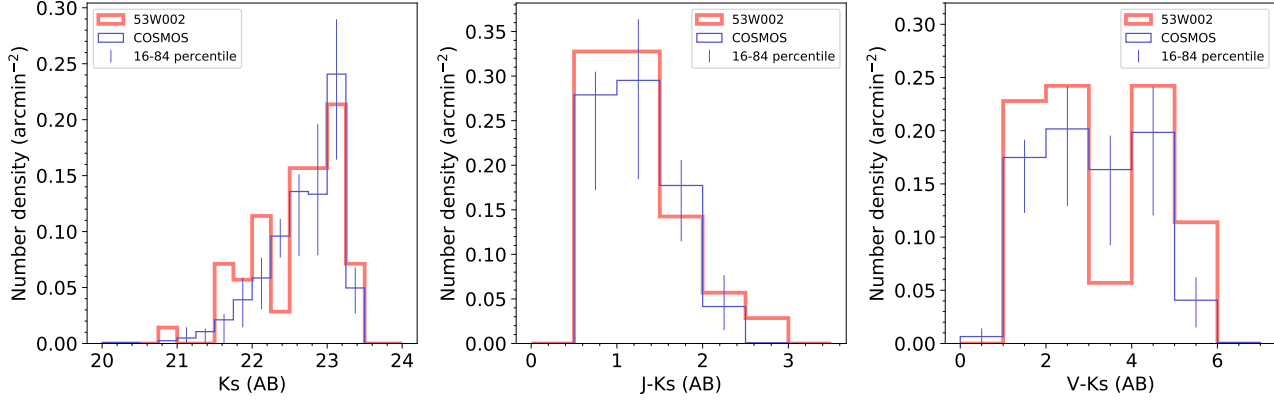


Figure 4. Left: K_s -band number counts of the JHK_s -selected galaxies in the 53W002 (red) and COSMOS (blue) fields. Error bars represent the 16 and 84 percentiles of the result in 100 random fields of view of $10' \times 10'$ in the COSMOS field (see text). Middle: $J - K_s$ color distribution of the selected galaxies in the 53W002 and COSMOS fields. The error bars are the same as in the left panel. Right: The same as the middle panel but for $V - K_s$ color.

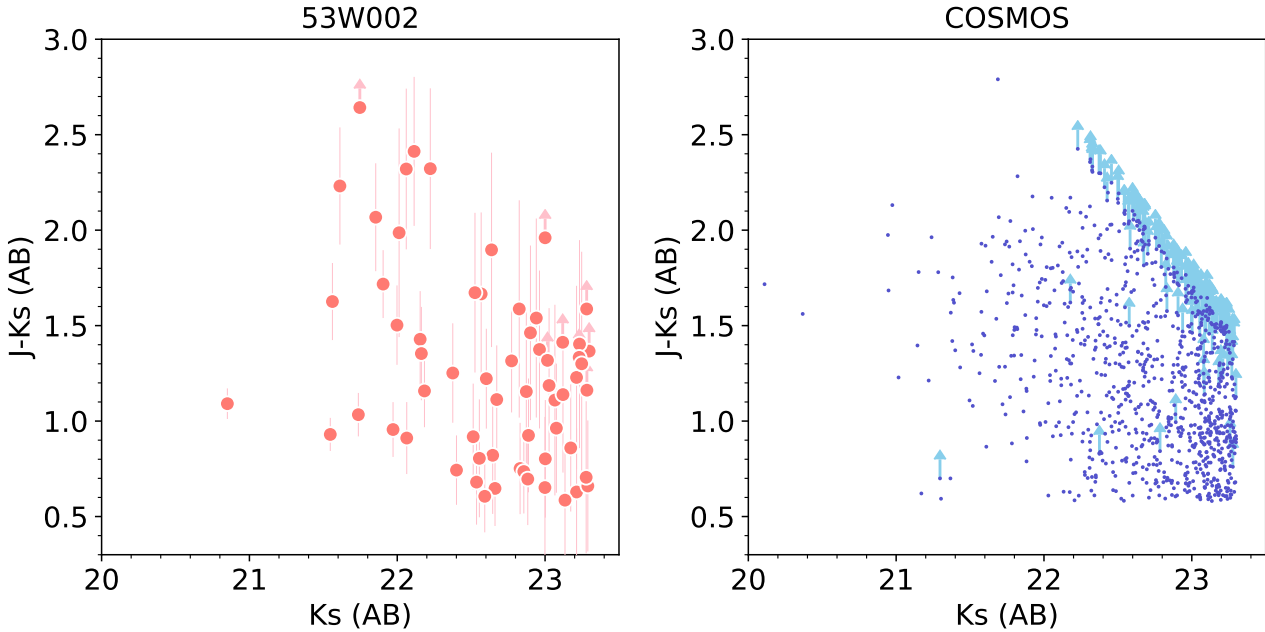


Figure 5. $J - K_s$ vs. K_s color-magnitude diagram for the JHK_s -selected galaxies in the 53W002 (left panel) and COSMOS (right) fields. The symbols with allows represent the lower limit of $J - K_s$ color. In the right panel, the error bars are omitted for clarity.

field, 83% of those with $M_s > 10^{10.5} M_\odot$ show $\text{sSFR} < 10^{-10} \text{ yr}^{-1}$, while 84% of those with $\text{sSFR} > 10^{-10} \text{ yr}^{-1}$ have $M_s < 10^{10.5} M_\odot$. Low-mass galaxies with $M_s \sim 10^{10} M_\odot$ show a variety of sSFR from $\lesssim 10^{-11} \text{ yr}^{-1}$ to $\gtrsim 10^{-8} \text{ yr}^{-1}$, although the uncertainty in their sSFR s is relatively large. One can see a group of massive galaxies with $M_s \gtrsim 10^{11} M_\odot$ and $\text{sSFR} \sim 10^{-10.5} - 10^{-10} \text{ yr}^{-1}$ in the 53W002 field. Their sSFR s suggest that their star formation has not yet stopped completely.

In order to directly compare the distribution in the sSFR vs. M_s plane and subtract the contribution of

field galaxies, we made a probability density distribution in this plane. First, we divided this plane into rectangular grids with an equal spacing in $\log M_s$ and $\log \text{sSFR}$, and searched a minimum χ^2 value in each grid in the SED fitting for each object after replacing data with $\text{sSFR} < 10^{-12} \text{ yr}^{-1}$ to $\text{sSFR} = 10^{-12} \text{ yr}^{-1}$. Next, we converted χ_{min}^2 for each grid into a probability of $P \propto e^{-\chi_{min}^2/2}$, which was normalized so that the summation over all grids equals to 1. Finally, we stacked the probability of all sample galaxies in each grid and then divided it by the survey area to obtain the probability

Table 3. Number densities for the JHK_s -selected galaxies with the different magnitude and color cuts.

Condition	Number density (arcmin ⁻²)					
	$K_s < 23.3$	$K_s < 22.25$	$J - K_s > 2$	$V - K_s > 4$	$J - K_s > 2$ & $K_s < 22.25$	$V - K_s > 4$ & $K_s < 22.25$
	53W002 field	0.88	0.27	0.085	0.36	0.085
COSMOS field	0.79	0.14	0.042	0.24	0.011	0.072
Reproduced rate ^a	12%	0%	13%	1%	0%	0%

^aThe fraction of random fields of view of $10' \times 10'$ in the COSMOS field with a higher number density than that in the 53W002 field.

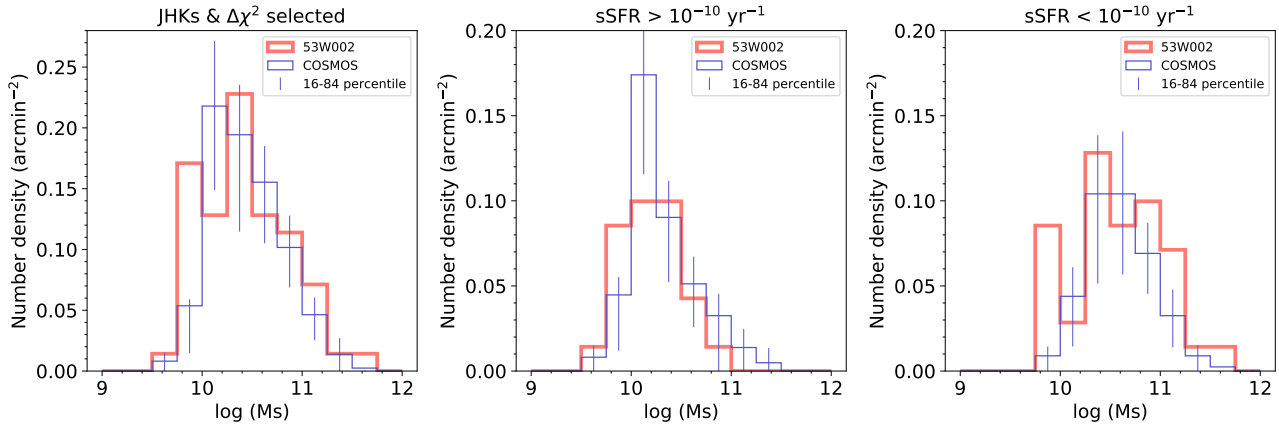


Figure 6. Left: Stellar mass distribution of the JHK_s -selected galaxies in the 53W002 (red) and COSMOS (blue) fields. The error bars are the same as in Figure 4. Middle: The same as the left panel but for those with $\text{sSFR} > 10^{-10} \text{ yr}^{-1}$. Right: The same as the left panel but for those with $\text{sSFR} < 10^{-10} \text{ yr}^{-1}$.

density distribution. Panels (c) and (d) of Figure 7 show the probability density distributions in the 53W002 and COSMOS fields, respectively. We subtracted the probability density distribution in the COSMOS field from that in the 53W002 field to derive probability density excess in the 53W002 field (panel (e) of Figure 7). There is a clear number density excess at $M_s \sim 5 \times 10^{10} - 10^{11} M_\odot$ and $\text{sSFR} < 10^{-11} \text{ yr}^{-1}$ in the 53W002 field. One can see also excesses at $M_s > 10^{11} M_\odot$ and $M_s < 10^{10} M_\odot$ in the probability density excess map. The panel (f) of Figure 7 shows the variation of the probability density distribution in random fields of view in the COSMOS field. The dispersion among random fields is about $0.003 - 0.005 \text{ arcmin}^{-2}$, and the excesses mentioned above are larger than the field-to-field variation, especially for quiescent galaxies with $M_s = 5 \times 10^{10} - 10^{11} M_\odot$ and $\text{sSFR} < 10^{-11} \text{ yr}^{-1}$. We note that the observed SEDs of the low-mass galaxies can be affected by strong emission lines such as [OIII] $\lambda\lambda 4959, 5007$ and $H\alpha$, which enters into H and K_s bands at $z \sim 2.39$. In fact, some of these

galaxies can also be fitted well with models with high sSFR of $\gtrsim 10^{-8} \text{ yr}^{-1}$ and strong emission lines (Appendix A). However the trend of the excess of low-mass galaxies with $M_s < 10^{10} M_\odot$ would not change significantly even if we include the nebular emission in the SED fitting as shown in the appendix. On the other hand, galaxies with $M_s = 1 - 5 \times 10^{10} M_\odot$ and $\text{sSFR} = 10^{-10} - 10^{-8} \text{ yr}^{-1}$ in the 53W002 field have a smaller number density than in the COSMOS field. Although the deficit may be within the field-to-field variation, it is also possible that there are few such intermediate-mass star-forming galaxies in this protocluster.

Panels (a)–(d) of Figure 8 show mass-weighted age vs. M_s and its probability density distribution. More massive galaxies tend to have older stellar ages in the both fields. In the 53W002 field, most of galaxies with $M_s > 5 \times 10^{10}$ show ages older than $10^{8.5} \text{ yr}$, and six of the seven massive galaxies with $M_s > 10^{11} M_\odot$ are older than 1 Gyr. On the other hand, low-mass galaxies with $M_s < 10^{10} M_\odot$ tend to show the mass-weighted

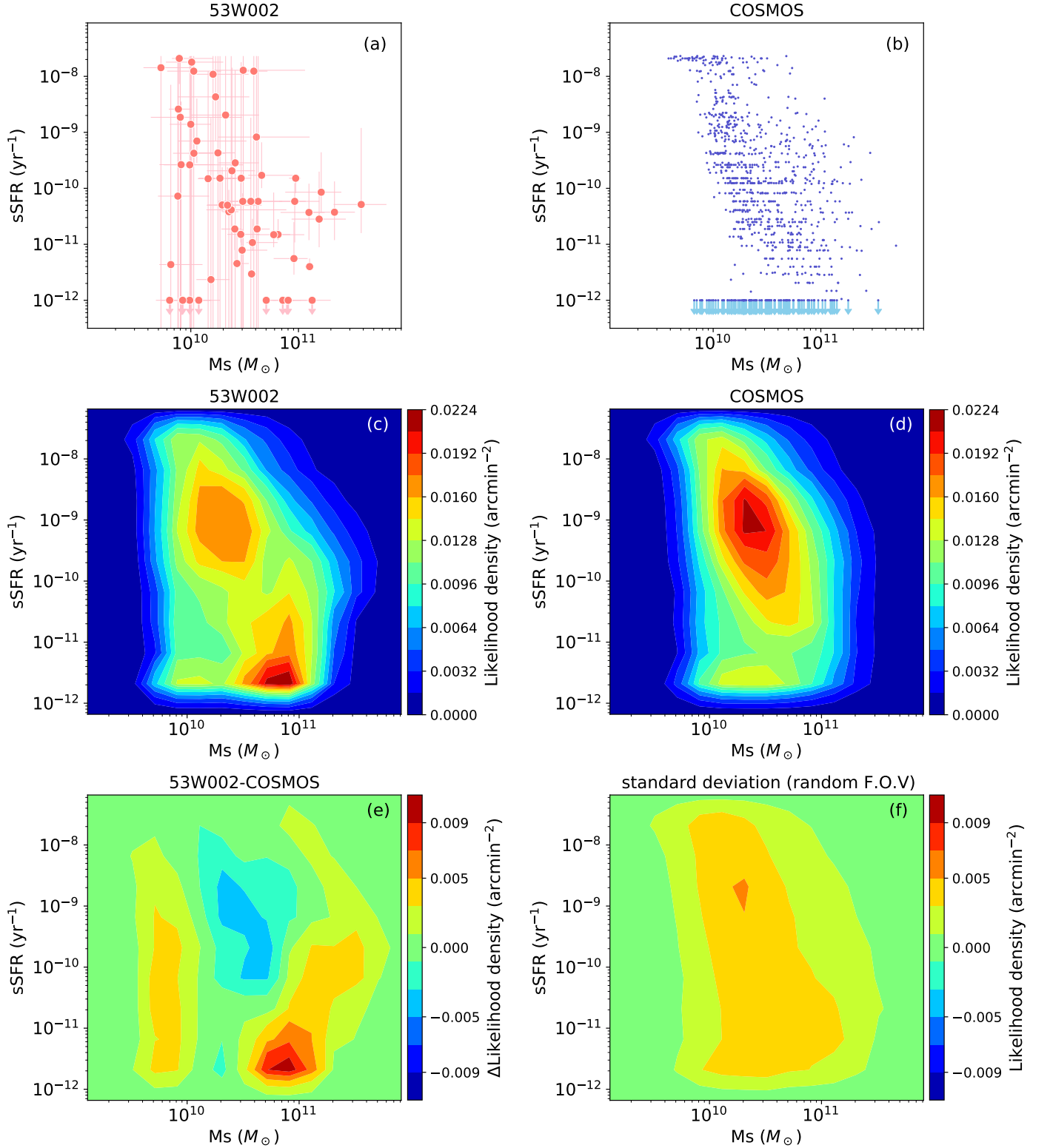


Figure 7. (a): sSFR vs. M_s for the JHK_s -selected galaxies in the 53W002 field. Symbols with arrows mean sSFR $< 10^{-12} \text{ yr}^{-1}$. (b): The same as the panel (a) but in the COSMOS field. Error bars are omitted for clarity. (c): Probability density distribution in sSFR vs. M_s for the selected objects in the 53W002 field. (d): The same as the panel (c) but in the COSMOS field. (e): Excess map of the probability density distribution in the 53W002 field, which is calculated by subtracting that in the COSMOS field. (f): Field variance of the probability density distribution for random fields of view of $10' \times 10'$ in the COSMOS field.

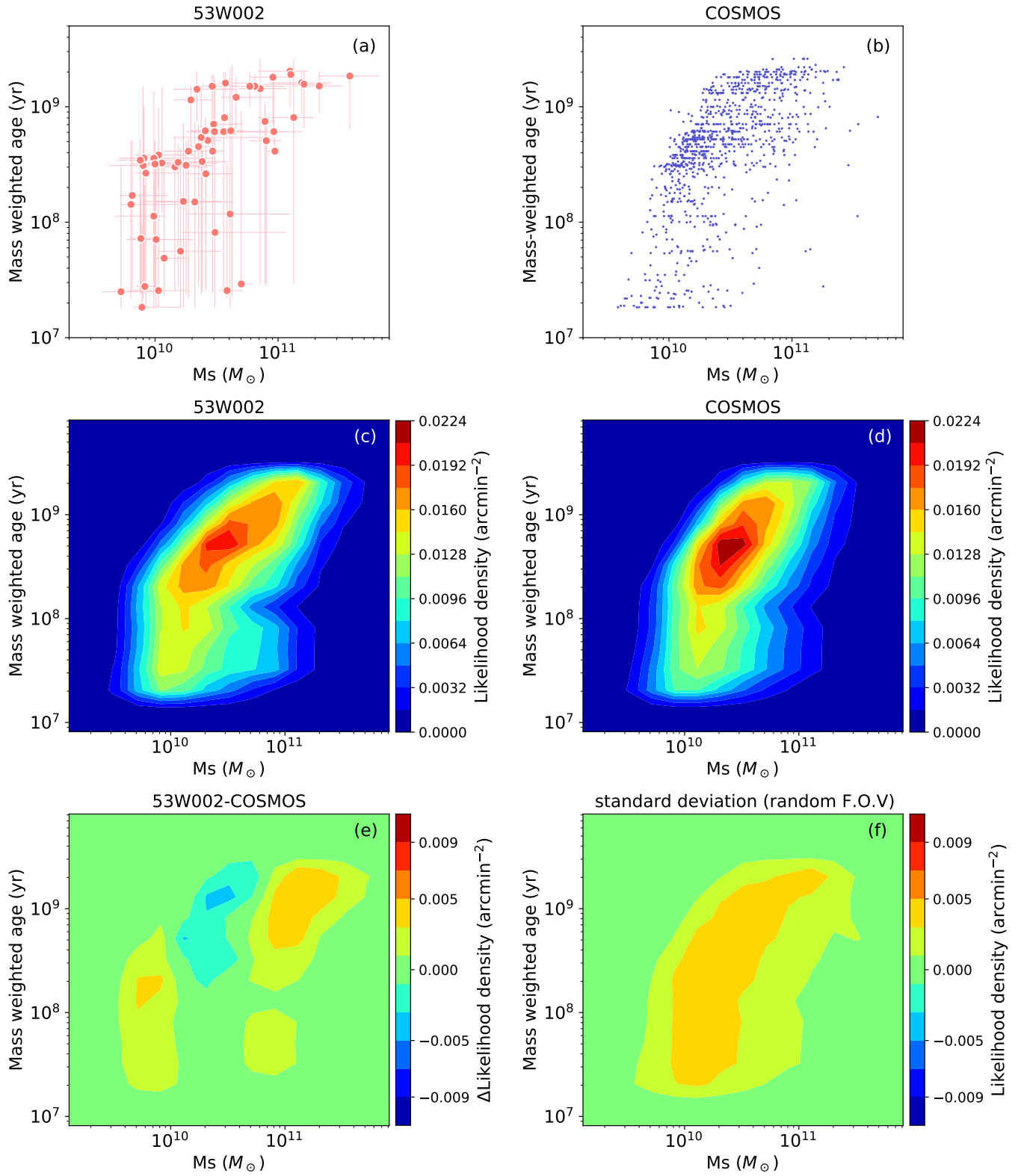


Figure 8. The same as Figure 7, but for mass-weighted age vs. M_s .

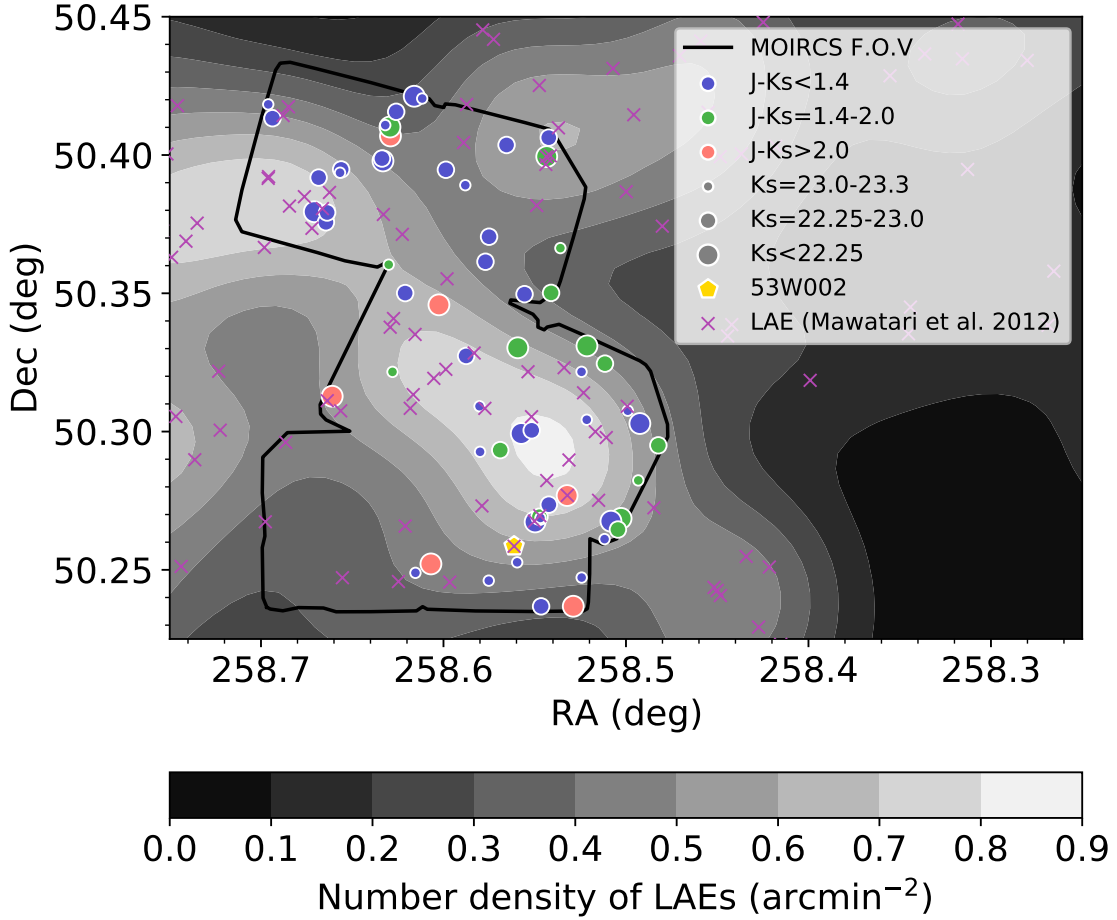


Figure 9. Spatial distribution of the JHK_s -selected galaxies (circles) and LAEs (crosses). The different colors of circle symbols represent objects with different $J - K_s$ colors, while the different sizes of the symbols show different K_s -band magnitudes. The yellow pentagon shows the radio galaxy 53W002. The grey-scale contour is the same as in Figure 2. The black line indicates our survey area observed with MOIRCS.

ages younger than $10^{8.5}$ yr, although the uncertainty of their age is relatively large. Panels (e) and (f) of Figure 8 show the similar probability density excess map in the 53W002 field as the panel (e) of Figure 7 and the variation of probability density among the random fields of view in the COSMOS field, respectively. The distributions in the two fields are different at $M_s > 10^{10.5} M_\odot$ and $< 10^{10} M_\odot$. In the excess at $M_s > 10^{10.5} M_\odot$, the expected age increases with increasing stellar mass, and the probability of age larger than 1 Gyr is high at $M_s > 10^{11} M_\odot$. At $M_s < 10^{10} M_\odot$, the probability excess ranges from 2×10^7 yr to 3×10^8 yr. On the other hand, there is a deficit at $M_s \sim 1-5 \times 10^{10} M_\odot$ and age $> 2 \times 10^8$ yr. We note that the field-to-field variation is relatively large in the mass-weighted age- M_s plane and it could affect the probability density excess mentioned above.

4.3. Overlap with LAEs

Figure 9 shows the sky distribution of the JHK_s -selected galaxies and LAEs discovered by Mawatari et al. (2012) in the 53W002 field. The symbol size and color of circles represent the different K_s -band total magnitudes and $J - K_s$ colors of the selected objects, respectively. The crosses and grey-scale contour show LAEs and their number density map. The yellow pentagon indicates the radio galaxy 53W002.

Since our NIR selection basically picks up with $M_s \gtrsim 10^{10} M_\odot$ and is complementary to the LAE selection, the fraction of such overlapping objects is expected to be small. Nevertheless there are three JHK_s -selected galaxies that are also selected as LAEs (overlapping circle and cross symbols in the figure). Interestingly, all the three objects have bright K_s -band magnitudes of $K_s < 22.25$. One is the object No.18 in Pascarelle et al. (1996b), which is located about $40''$ northwest of 53W002 and one of the spectroscopically confirmed protocluster members at $z = 2.393$. Its rest-UV and optical

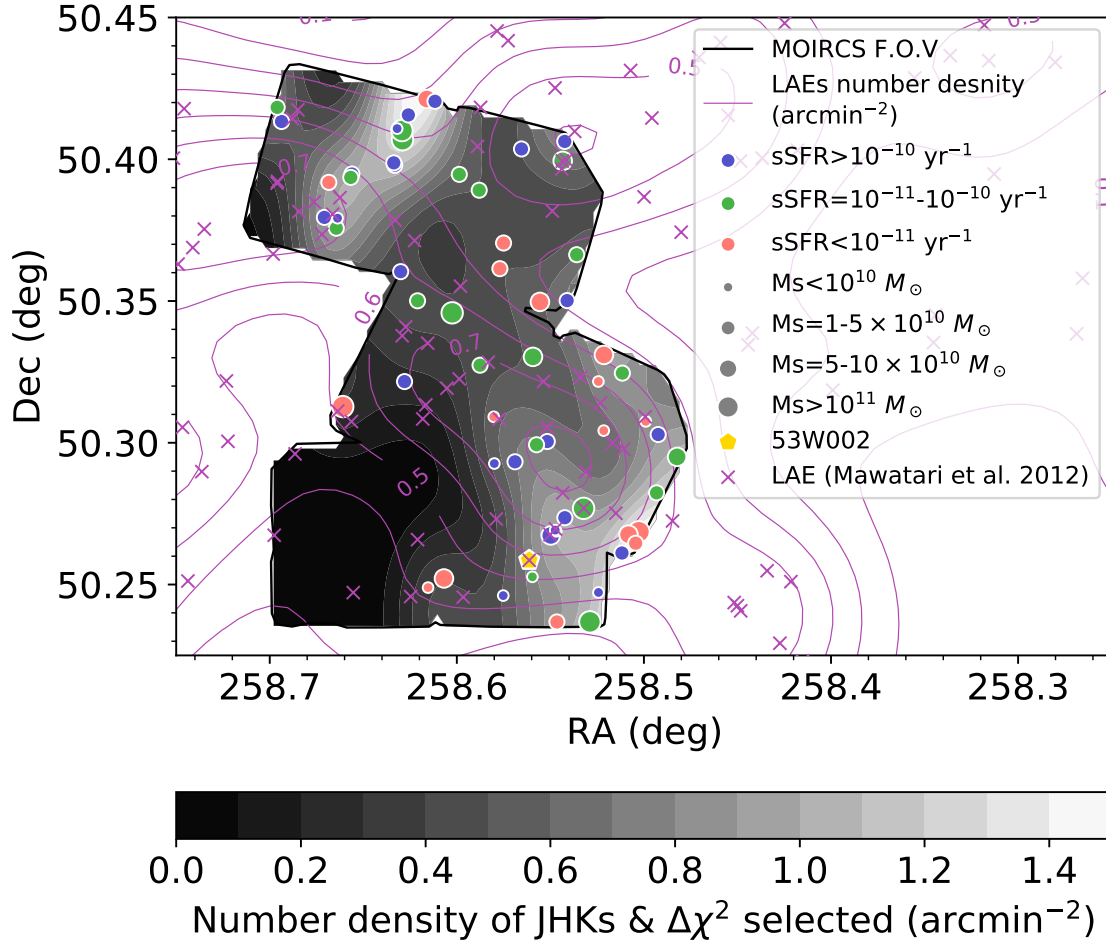


Figure 10. The same as Figure 9, but different symbol colors and sizes represent the different sSFRs and stellar mass of the JHK_s -selected galaxies. The grey scale contour shows the number density of the JHK_s -selected galaxies smoothed by a Gaussian kernel with $\sigma = 1.0$, which corresponds to ~ 1.7 cMpc at $z = 2.39$. The purple contour shows the number density of LAEs.

emission lines indicate the AGN contribution (Pascarelle et al. 1996a; Motohara et al. 2001), and it has the very extended Ly α emission (Mawatari et al. 2012). The estimated stellar mass is large ($9.4 \times 10^{10} M_\odot$), and its relatively blue color of $J - K_s \sim 1.1$ may be affected by the AGN emission. The second object is located about 50 arcsec northwest of the No.18. This object has a red color of $J - K_s = 2.2$ and a very large stellar mass of $2.1 \times 10^{11} M_\odot$. Its estimated sSFR is intermediate ($10^{-10.6} \text{ yr}^{-1}$) with a moderate extinction of $E(B - V) = 0.18$. These properties suggest that its Ly α emission may be also related with AGN, although we need spectroscopy to confirm it. The third object is located near the northwest corner of FOV3. It has a stellar mass of $M_s = 6.5 \times 10^{10} M_\odot$ and a relatively low sSFR of $10^{-10.8} \text{ yr}^{-1}$. Interestingly, a Lyman α blob discovered by Mawatari et al. (2012) is located within $\sim 10''$ from this object. These three objects have large

stellar mass and old stellar age, which is different from typical LAEs.

We note that another faint JHK_s -selected galaxy with $K_s = 22.9$ lies $1''.5$ from LAE No.19 in Pascarelle et al. (1996b) that is located about $10''$ northwest of the No.18. The No.19 is QSO at $z = 2.39$ (Pascarelle et al. 1996a), and has a bright corresponding source in the K_s band ($K_s = 20.3$), which dose not satisfy the JHK_s -color criteria probably due to the strong AGN emission. The extended Ly α emission of the No.19 (Mawatari et al. 2012) seems to cover this object, and this may be a companion of the No.19.

4.4. Spatial Distribution

We here investigate the spatial distribution of the JHK_s -selected galaxies and compare with LAEs discovered by Mawatari et al. (2012). In Figure 9, the JHK_s -selected galaxies are distributed over our survey field except for southeast region (eastern half of FOV1),

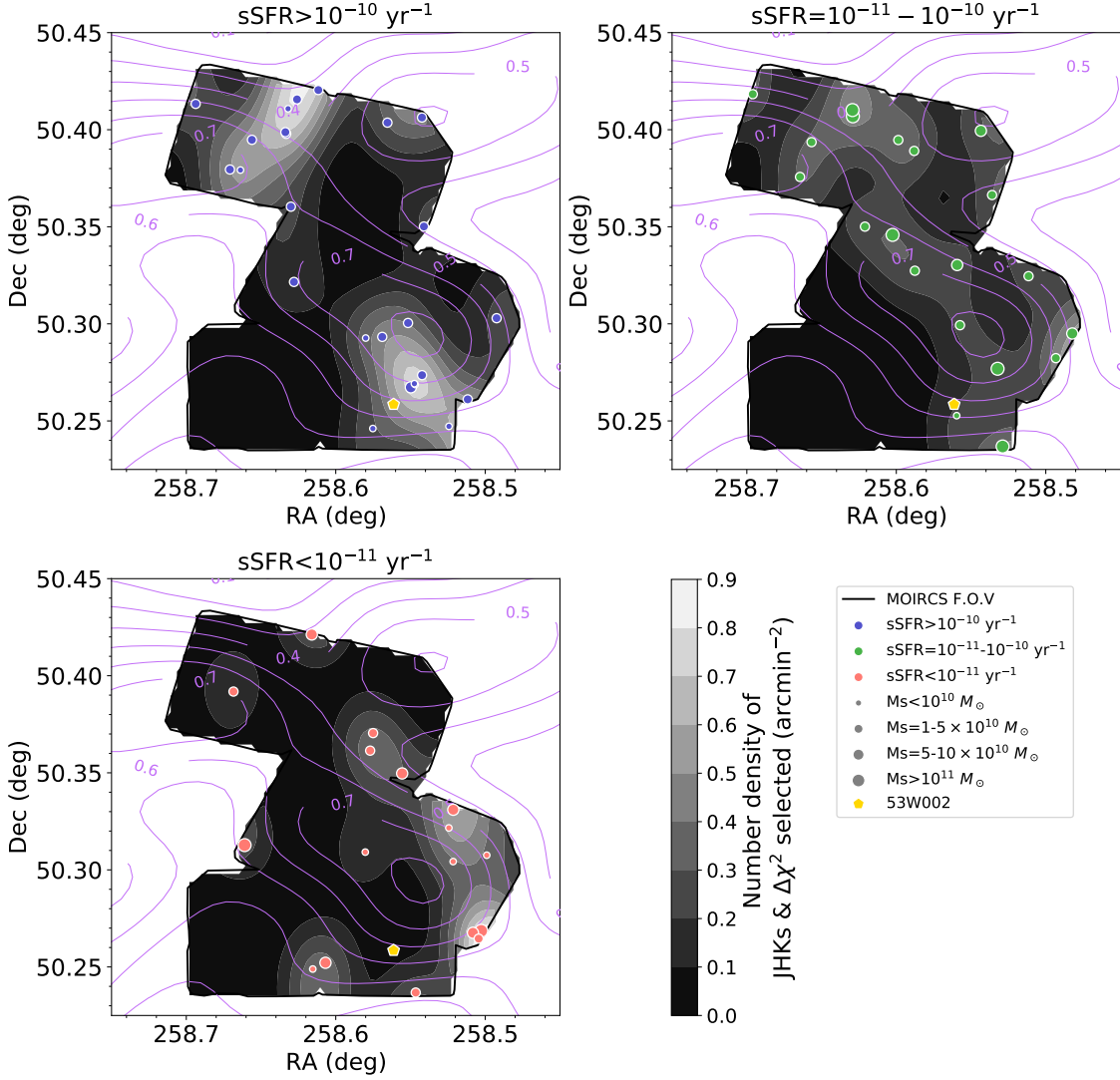


Figure 11. The same as Figure 10, but the selected galaxies with different sSFRs are shown separately in the different panels (upper left: $sSFR > 10^{-10} \text{ yr}^{-1}$. upper right: $sSFR = 10^{-11} - 10^{-10} \text{ yr}^{-1}$. lower left: $sSFR < 10^{-11} \text{ yr}^{-1}$). Note that the scale of grey-scale contour is changed from the Figure 10.

where the number density of the LAEs is also low. The radio galaxy 53W002 is located at outskirts of the density peak of LAEs, and there are few bright and red galaxies in vicinity of 53W002, which is consistent with the previous study of Yamada et al. (2001). In Figure 10, we show the distribution of the JHK_s -selected galaxies and their number density map with the grey scale. While their distribution is widespread, there are two high-density regions of those galaxies. One is located at southwest region of our survey field, namely, $RA=258^{\circ}52$, $Dec=50^{\circ}27$. The other is located at northern region of the survey field, $RA=258^{\circ}62$, $Dec=50^{\circ}42$. Interestingly, these two density peaks are spatially offset from the two density peaks of LAEs in our survey field by 2–2.5 arcmin ($\sim 1-1.2$ physical Mpc at $z = 2.39$). The structure of the JHK_s -selected galaxies in and around

the both high-density regions extend toward these density peaks of LAEs.

We also investigated how the spatial distribution of the JHK_s -selected galaxies depends on their sSFRs. Figure 11 shows the distributions of those galaxies with different sSFRs, separately. The distribution of those with $sSFR > 10^{-10} \text{ yr}^{-1}$ show two clear structures from the high-density regions to the density peaks of LAEs mentioned above. Most of these star-forming galaxies seem to belong to these structures. There are also two galaxies in the northwest part of FOV3 where the LAE density increases. On the other hand, quiescent galaxies with $sSFR < 10^{-11} \text{ yr}^{-1}$ tend to avoid the high-density region of LAEs. Many such galaxies are distributed west and north of the southwest high-density peak of LAEs. Most of the other quiescent galaxies are also located rel-

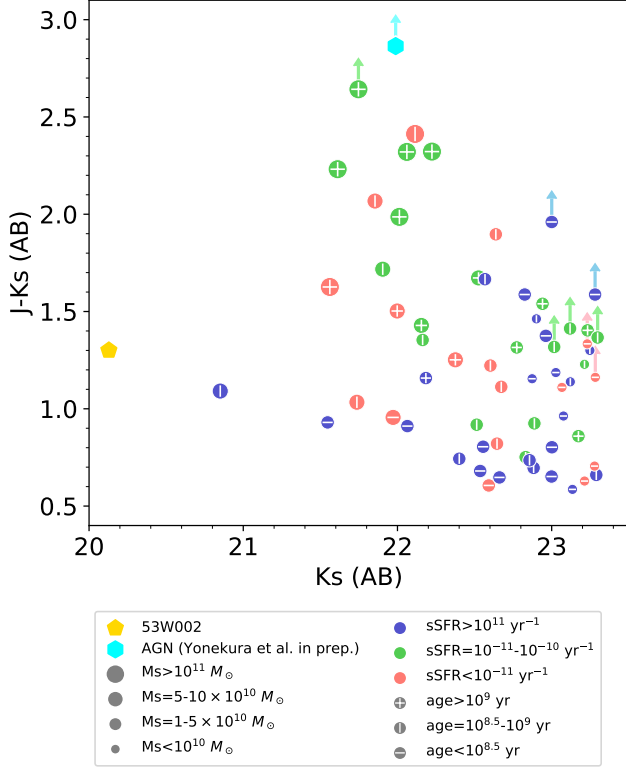


Figure 12. $J - K_s$ vs. K_s color magnitude diagram for the JHK_s -selected galaxies in the 53W002 field. The different colors and sizes of symbols represent their sSFRs and stellar mass, while cross, vertical, and horizontal lines mean the different mass-weighted ages. The yellow pentagon and cyan hexagon indicate the radio galaxy 53W002 and AGN (see text), respectively.

actively low-density regions of LAEs. The distribution of those with $sSFR = 10^{-11} - 10^{-10} \text{ yr}^{-1}$ overlaps with the both star-forming and quiescent galaxies mentioned above, and they are distributed over the entire survey field except for the southeast part.

5. DISCUSSION

5.1. Bright and Red Galaxies

We found that the JHK_s -selected galaxies with bright K_s -band magnitudes and/or red $J - K_s/V - K_s$ colors show the number density excesses in the 53W002 field (Figure 4). In particular, those galaxies with $K_s < 22.25$ and $J - K_s > 2$ show about eight times higher number density than in the COSMOS field (Table 3). In Figure 12, we plot the selected galaxies with different M_s , sSFRs, and mass-weighted ages by different symbols on the $J - K_s$ vs. K_s plane. Five out of the six galaxies with $K_s < 22.25$ and $J - K_s > 2$ have $M_s > 10^{11} M_\odot$, and the stellar mass of the other one is $8 \times 10^{10} M_\odot$. There are additional two massive galaxies with $M_s > 10^{11} M_\odot$,

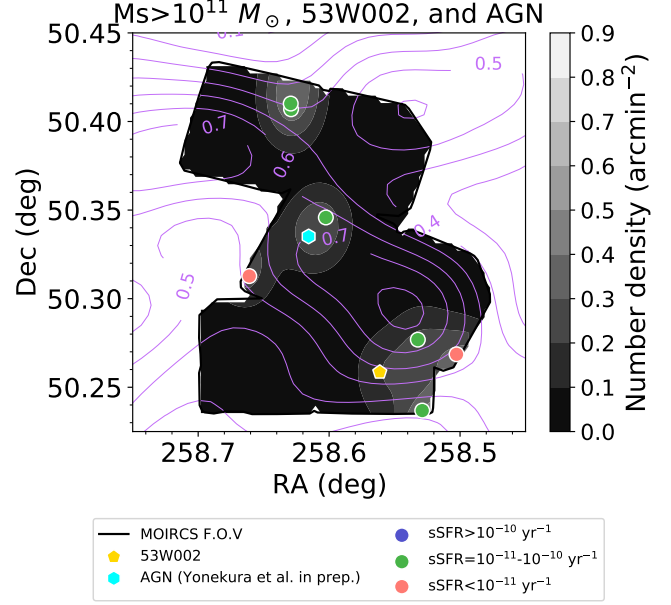


Figure 13. The same as the Figure 10, but the selected galaxies with $M_s > 10^{11} M_\odot$ and other massive galaxies are shown. The yellow pentagon and cyan hexagon indicate the radio galaxy 53W002 and AGN (see text), respectively. The grey contour show the number density of not only selected massive galaxies but also 53W002 and AGN.

which do not satisfy $J - K_s > 2$, but have similarly bright magnitudes and red colors. Most of these galaxies show old mass-weighted stellar ages of 1.5–2.0 Gyr. On the other hand, their sSFRs are intermediate values of $10^{-11} - 10^{-10} \text{ yr}^{-1}$, which suggests that their star formation has not completely stopped. Their best-fit dust extinction values are $E(B - V) = 0.18 - 0.42$, and their very red colors of $J - K_s > 2$ are caused by combination of the old stellar population and dust extinction. We note that there are two more protocluster members with similarly large stellar mass of $\gtrsim 10^{11} M_\odot$. One is the radio galaxy 53W002 whose estimated stellar mass is $\sim 1.8 \times 10^{11} M_\odot$, although the strong emission from AGN could affect our estimation with the SED fitting. The other object was selected by the JHK_s -color criteria, but was not included in our sample because its $\Delta\chi^2_{z=2.39}$ is large probably due to strong emission lines. This object is also one of LAEs selected by Mawatari et al. (2012), and we confirmed very strong $[\text{OIII}]\lambda\lambda 4959, 5007$ emission lines at $z = 2.39$ in its NIR spectrum, which suggests this object also has AGN (Yonekura et al. in prep.).

We consider that such many massive galaxies with $M_s > 10^{11} M_\odot$ are associated with this protocluster because of the very high number density, which cannot be seen in the COSMOS field. Figure 13 shows their

spatial distribution. Their spatial distribution does not concentrate on some position in the protocluster, but they are rather widely distributed along a SW-NE direction. The position angle of their distribution seems to be offset from that of the structure of LAEs, and these massive galaxies are not located at the high-density peaks of LAEs, but slightly lower densities of LAEs. These massive galaxies have old stellar ages but have not yet stopped their star formation completely, and some of these have AGN activity as mentioned above. On the other hand, most of LAEs are expected to be young and formed very recently. In this structure along the SW-NE direction, there might be large-scale gas supply, which leads to the coherent formation of LAEs and maintenance of the activities in massive galaxies (Section 5.5).

If this protocluster evolves into a massive cluster at lower redshift, these massive galaxies with $M_s > 10^{11} M_\odot$ are expected to form the bright end of the red sequence. At $z = 2.39$, they show a large scatter in $J - K_s$ color probably due to their star formation and dust extinction despite of their old mean age, and their $J - K_s$ colors seem to be too red for the red sequence at $z \sim 2.4$ (Kodama et al. 2007). In fact, (slightly less massive) quiescent galaxies with similarly old ages show $J - K_s \sim 1.5$ (Figure 12). If the star formation in the massive galaxies would stop as this structure grows and collapses, these massive galaxies with very red colors will lose gas and dust and concentrate on the red sequence.

5.2. Quiescent Galaxies

In addition to the most massive galaxies with $M_s > 10^{11} M_\odot$, we also found the density excess of relatively massive quiescent galaxies with $M_s = 5 \times 10^{10} - 10^{11} M_\odot$ and $\text{sSFR} < 10^{-11} \text{ yr}^{-1}$ in the 53W002 field (panel (e) of Figure 7). Their mass-weighted stellar ages are $\sim 0.5 - 2.0$ Gyr. They show a variety of $J - K_s$ color depending on their stellar age and dust extinction (Figure 12), while those with old stellar ages of $\gtrsim 1$ Gyr tend to have $J - K_s \sim 1.5$ as mentioned above. The sSFRs of these quiescent galaxies are systematically lower than those of field galaxies with similar stellar masses of $5 \times 10^{10} - 10^{11} M_\odot$ in the COSMOS field (panels (c) and (d) of Figure 7). While we fixed the redshift to $z = 2.39$ in the SED fitting for these field galaxies to subtract their contribution from the results in the 53W002 field, the estimated M_s , sSFR, and mass-weighted age do not significantly change if we adopt the photometric redshift estimated with more than 30 bands from the COSMOS2015 catalog in the SED fitting and select only those at $z_{\text{photo}} = 2.39 \pm 0.20$ (Appendix B). On the other hand, the mass-weighted ages of these quiescent

galaxies in the 53W002 field are similar with those of field galaxies with similar mass. Therefore, these quiescent galaxies may have experienced similar star formation histories with field galaxies in the past and then stop their star formation recently, for example, hundreds Myr before the observed epoch. These quiescent galaxies tend to avoid the high-density region of LAEs, and many of them located north and west of southwest density peak of LAEs (lower left panel of Figure 11). Interestingly, most of low-mass quiescent galaxies with $M_s < 10^{10} M_\odot$ and $\text{sSFR} < 10^{-11} \text{ yr}^{-1}$ are also located in the same region. They show a young stellar age of $\lesssim 10^{8.5} \text{ yr}$ and $E(B - V) \sim 0$, which is similar with low-mass star-forming galaxies with $M_s < 10^{10} M_\odot$ and $\text{sSFR} > 10^{-10} \text{ yr}^{-1}$. Therefore, their lower sSFRs are probably caused by recent quenching of star formation. While quiescent galaxies with $M_s \lesssim 10^{11} M_\odot$ are located in this region, we do not know how far the region of quiescent galaxies extends due to our limited survey area. There may be a massive structure or main halo west of our survey area, where some mechanisms such as starburst by merger/interaction, starvation, or tidal/ram-pressure stripping might work well (e.g., Muldrew et al. 2018).

5.3. Low-Mass Star-Forming Galaxies

The low-mass galaxies with $M_s < 10^{10} M_\odot$ also show the higher number density than those galaxies with the similar stellar mass in the COSMOS field. The number density excess of low-mass galaxies can be seen over a wide range of sSFR (Figures 6 and 7). Although the excess of low-mass galaxies with $\text{sSFR} > 10^{-10} \text{ yr}^{-1}$ is less significant than those with $\text{sSFR} < 10^{-10} \text{ yr}^{-1}$, these low-mass star-forming galaxies are distributed over the structures between the high-density region of the JHK_s -selected galaxies and the peak of LAEs (Figure 11), which suggests that many of these galaxies are associated with this protocluster. These star-forming galaxies have young mass-weighted ages of $\lesssim 10^{8.5} \text{ yr}$ and very small dust extinction (median value of $E(B - V) = 0.02$). These properties are similar with LAEs, while most LAEs are expected to have much smaller mass and younger age (e.g., Overzier et al. 2008; Ono et al. 2010; Hagen et al. 2014; Shimakawa et al. 2017a). Such similarity in the physical properties may be related with the overlapping spatial distribution of these galaxies and LAEs.

5.4. Intermediate-Mass Galaxies

While massive or low-mass galaxies show the number density excesses in the 53W002 field as described above, the number density of the JHK_s -selected galaxies with

$1\text{--}5 \times 10^{10} M_{\odot}$ in the 53W002 field is smaller than that in the COSMOS field. Since the field-to-field variation is relatively large in this stellar mass range for our selection method (panel (f) of Figure 7), the lower density of these galaxies could be explained by the field variation of foreground/background galaxies. Otherwise, the deficit of these intermediate-mass galaxies may occur in this protocluster. Shi et al. (2021) reported the similar bimodal number density excess in the stellar mass function and deficit between the massive and low-mass excesses in a protocluster originally selected by a number density excess of LBGs at $z = 3.24$, although the deficit of galaxies occurs at more massive stellar mass of $10^{10.6}\text{--}10^{11} M_{\odot}$. If this is the case in the 53W002 protocluster, some mechanism decreasing their number density such as active mergers and/or disruption in earlier time (e.g., Muldrew et al. 2018) may be required because the stellar mass function of galaxies at similar redshifts in general fields does not show such deficit (e.g., Kajisawa et al. 2009; Ilbert et al. 2013). However, the wide spatial distribution of massive galaxies with $M_s > 10^{11} M_{\odot}$ along the SW-NE direction may be difficult to reconcile with such scenario where most of these intermediate-mass galaxies had been merged into massive galaxies.

5.5. Comparisons with Previous Studies

We searched massive galaxies with the optical-NIR photometric data in the field of the high-density structure of LAEs at $z = 2.39$ near the radio galaxy 53W002, and found the significant number density excess of massive galaxies with $M_s > 10^{11} M_{\odot}$ as well as quiescent galaxies with $M_s = 5 \times 10^{10}\text{--}10^{11} M_{\odot}$ and low-mass galaxies with $M_s < 10^{10} M_{\odot}$. Our result indicates a possibility that such high-density structures of LAEs, which tend to be low-mass and young galaxies, can trace protoclusters which include more massive galaxies. Previously, Uchimoto et al. (2012) and Kubo et al. (2013) carried out the similar search for massive galaxies in the high-density region of LAEs at $z = 3.09$ in the SSA22 field (Hayashino et al. 2004; Yamada et al. 2012), and found a significant number density excess of massive galaxies along the structure of LAEs, which includes a concentration of quiescent galaxies near the density peak of LAEs. The structure of LAEs in the SSA22 field has large extent (~ 60 comoving Mpc) and very high density peak (Yamada et al. 2012). Mawatari et al. (2012) reported that the overdensity of LAEs in the SSA22 protocluster corresponds to a rareness probability of 0.0017%, while that of LAEs in the 53W002 field is 0.9%. Shi et al. (2019a) also searched massive galaxies in a rich protocluster of LAEs at $z = 3.78$,

which was originally discovered as a concentration of five bright LBGs at $z = 3.78$ (Lee et al. 2013, 2014; Dey et al. 2016), and found a significant high-density structure of photo- z selected star-forming galaxies and a number density excess of color-selected Balmer break galaxies with $M_s > 10^{11} M_{\odot}$. Our discovery of the number density excess of massive galaxies in the 53W002 field suggests that even more moderate high-density structures of LAEs could trace protoclusters with many massive galaxies.

The similar searches for massive galaxies in protoclusters of LAEs have also been done in the fields of high-redshift powerful radio galaxies at $z \sim 2\text{--}3$ (Kurk et al. 2004; Kodama et al. 2007). These studies found number density excesses of NIR-selected (massive) galaxies in the protoclusters of LAEs, which had been discovered by the narrow-band search around the radio galaxies (Venemans et al. 2007). Kodama et al. (2007) found that massive galaxies tend to be located along the structure of LAEs. We note that such powerful radio galaxies at high redshift are preferentially located in high-density environments (e.g., Hatch et al. 2014), and therefore the overdensity of massive galaxies in these studies may be closely related with the radio galaxies rather than the structure of LAEs. While massive galaxies and LAEs in these protoclusters are distributed around the powerful radio galaxies, the radio galaxy 53W002 is located at outskirts of the high-density structures of both LAEs and JHK_s -selected galaxies. The distribution of these massive galaxies in the 53W002 field seems to be related with the structures of LAEs rather than the radio galaxy.

Several previous studies reported the spatial segregation between LAEs and more massive galaxies in protoclusters at the similar redshifts (e.g., Yang et al. 2010; Shimakawa et al. 2017b; Shi et al. 2019a, 2020). Shimakawa et al. (2017b) reported that LAEs distribute so as to avoid the most high-density regions of more massive H α emitters in a protocluster, which consists of large number of star-forming galaxies at $z = 2.53$ (Hayashi et al. 2012). Shi et al. (2019a) found that a peak position of the overdensity of photo- z selected (relatively massive) star-forming galaxies is offset from the high-density region of LAEs, and color-selected quiescent galaxies also avoid the overdensity of LAEs. Shi et al. (2020) reported that photo- z selected (massive) quiescent galaxies are segregated from the high-density region of LAEs, while less-dusty star-forming galaxies with relatively low stellar mass coexist with LAEs in the high-density region. In the 53W002 field, the high-density peaks of the JHK_s -selected galaxies are offset from the density peaks of LAEs, and the distribution of

star-forming galaxies with $s\text{SFR} > 10^{-10} \text{ yr}^{-1}$ extends to the peaks of LAEs, which is similar with the results of previous studies. Furthermore, the quiescent galaxies with $s\text{SFR} < 10^{-11} \text{ yr}^{-1}$, which include low-mass galaxies with $M_s < 10^{10} M_\odot$, are located avoiding the structure of LAEs (Figure 11). Such segregation may be caused by different evolutionary phase/mass assembly histories of different dark matter halos in the proto-cluster (e.g., Muldrew et al. 2018; Shi et al. 2019b). For example, Muldrew et al. (2018) studied the evolution of galaxies in protoclusters with their semi-analytic model, and proposed that the quenching of low-mass galaxies could occur mainly in a main (the most massive) halo in protoclusters at $z > 2$. The region dominated by quiescent galaxies seen in Figure 11 may be associated with such a massive halo in the protocluster.

On the other hand, some specific conditions are required for the formation of structures of LAEs, since LAEs tend to show weaker clustering in their spatial distribution than massive and/or quiescent galaxies and avoid high-density regions such as protoclusters (e.g., Ouchi et al. 2010; Kusakabe et al. 2018; Khostovan et al. 2019; Ito et al. 2021). First, LAEs are generally very young as mention above, and therefore those galaxies in the structures are expected to be almost simultaneously formed very recently, which may need the recent cold gas supply over a scale of such structure. Furthermore, the HI and dust column densities should be sufficiently low so that we can observe their Ly α emission (e.g., Shimakawa et al. 2017b). In fact, several studies reported that the large-scale (tens of Mpc) HI gas traced by Ly α absorption is associated with high-density structures of LAEs (Cucciati et al. 2014; Mawatari et al. 2017; Liang et al. 2021), while the high optical depth of Ly α emission could lead to a deficit of LAEs at small scale (e.g., Momose et al. 2021a,b). The most massive galaxies with $M_s > 10^{11} M_\odot$ in the 53W002 field are offset from high-density peaks of LAEs, but they show the similar wide distribution along the SW-NE direction (Figure 13). While they have old mass-weighted stellar ages of 1.5–2.0 Gyr, their intermediate sSFRs of 10^{-11} – 10^{-10} yr^{-1} suggest that their star-formation activity has not yet stopped. In contrast, several studies reported that such massive protocluster members tend to be quiescent galaxies with lower sSFRs (e.g., Tanaka et al. 2010; Kubo et al. 2013, 2015, 2021; Ando et al. 2020; Chartab et al. 2020; Shi et al. 2021). Such star formation in the massive galaxies in the 53W002 field may be explained by the large-scale gas supply along the structure of LAEs.

The number density excess of the JHK_s -selected galaxies in the 53W002 field is significant at high stel-

lar mass of $\gtrsim 10^{11} M_\odot$, while low-mass galaxies with $M_s \lesssim 10^{10} M_\odot$ also show the excess. Several previous studies found that the stellar mass distribution of galaxies in protoclusters is skewed toward higher stellar mass (more top heavy) than field galaxies at the same redshifts (e.g., Cooke et al. 2014; Steidel et al. 2005; Hatch et al. 2011b; Shimakawa et al. 2018; Ando et al. 2020; Koyama et al. 2021). Theoretical models also predict that high abundance of massive dark matter halos in high-density regions such as protoclusters promotes the early and active formation of massive galaxies, because the sufficiently high density in such halos enables to form stars even in early epoch (the biased galaxy formation) and the high merger rate among halos in such regions drives stellar mass growth of galaxies (Lovell et al. 2018; Muldrew et al. 2018). The number density excess of massive galaxies in the 53W002 field seems to be consistent with such a scenario. Their old ages (1.5–2.0 Gyr) and relatively low sSFRs (10^{-11} – 10^{-10} yr^{-1}) suggest that the formation of massive galaxies has been advanced in this protocluster, while some previous studies discovered massive actively star-forming galaxies in other protoclusters (e.g., Cooke et al. 2014; Shimakawa et al. 2018; Koyama et al. 2021). Since these galaxies with $M_s > 10^{11} M_\odot$ are distributed over a scale of ~ 15 – 20 comoving Mpc, they are probably associated with different dark matter halos. Many of them may be still central galaxies at the observed epoch, whose moderate (or declining) star formation activity may be maintained by the large-scale gas supply mention above.

6. SUMMARY

In this paper, we searched massive galaxy candidates using the optical–NIR imaging data in the 53W002 protocluster field which had been discovered as the overdensity of LAEs at $z = 2.39$. We used the JHK_s -band color cuts and additional criterion from the photometric redshift analysis to make the sample of galaxy candidates at $z = 2.39$. We also made the comparison sample in the general field from the COSMOS2015 catalog with the same selection method and compared the statistical properties of the selected galaxies. Our main results are as follows:

- 62 and 976 galaxies with $K_s < 23.3$ were selected in the 53W002 and COSMOS fields, respectively. The number density of the JHK_s -selected galaxies in the 53W002 field is significantly higher than that in the COSMOS field at $K_s < 22.25$, $J - K_s > 2$, or $V - K_s > 4$. In particular, the number density of those with $K_s < 22.25$ and $J - K_s > 2$ is eight times higher than that in the general field.

- Our SED fitting analysis suggests that the objects with $K_s < 22.25$ and $J - K_s > 2$ have stellar mass of $M_s > 10^{11} M_\odot$. While their mass-weighted ages are ~ 1.5 – 2.0 Gyr, they show moderate sSFRs of 10^{-11} – 10^{-10} yr^{-1} and dust extinction.
- Furthermore, we also found the number density excess for the quiescent galaxies with $M_s = 5 \times 10^{10}$ – $10^{11} M_\odot$ and $\text{sSFR} < 10^{-11} \text{ yr}^{-1}$, and for low-mass galaxies with 5×10^9 – $10^{10} M_\odot$ over a wide range of sSFR.
- The spatial distribution of the selected galaxies by their colors and the SED fitting properties strongly depends on their M_s and sSFR. The massive galaxies with $M_s > 10^{11} M_\odot$ are offset from the density peaks of LAEs, but show the similar wide distribution along the SW-NE direction with the structure of LAEs. Quiescent galaxies with $M_s < 10^{11} M_\odot$ and $\text{sSFR} < 10^{-11} \text{ yr}^{-1}$ clearly avoid the overdensity regions of LAEs, and many such galaxies are located in the western part of the survey area. On the other hand, the distribution of low-mass star-forming galaxies with sSFR

$> 10^{-10} \text{ yr}^{-1}$ overlaps with the density peaks of LAEs.

While our results suggest that massive galaxies are abundant in the protocluster selected by the relatively moderate high-density structure of LAEs, we definitely need spectroscopic confirmation for the membership of those galaxies in this field. Furthermore, we here studied only one protocluster, and more investigations are needed for understanding the high-density structures of LAEs and formation of massive galaxies in protoclusters.

The imaging data used in this paper were taken with the Subaru Telescope, which is operated by National Astronomical Observatory of Japan (NAOJ). Data analysis in this paper was carried out on the Multi-wavelength Data Analyssi System operated by the Astronomy Data Center (ADC), NAOJ. This work was financially supported by JSPS (17K05386). K. M. is supported by JSPS KAKENHI grant No.20K14516.

APPENDIX

A. EFFECTS OF THE NEBULAR EMISSION

A.1. Sample Selection

In this subsection, we checked the effects of including the nebular emission in the model templates on the sample selection. We used the model spectra of PANHIT (Mawatari et al. 2020), which consist of the stellar component constructed by Bruzual & Charlot (2003) population synthesis and the nebular emission component by the Inoue (2011) model. The nebular emission is calculated from the ionizing photon production rate of the stellar component under the assumption of the same metallicity with the stellar component, typical ranges of hydrogen number density and ionizing parameter, plane-parallel geometry, and the escape fraction of ionizing photon of fC (Inoue 2011). For example, when fC is 0.0, all produced ionizing photons are used for ionization. On the other hand, when fC is 1.0, no ionizing photons are used. We assumed 4 kinds of fC of 0.0, 0.5, 0.9, and 1.0. Other parameters are the same values described in Section 3.1. We carried out the SED fitting with the models described above and selected the sample by using the JHK_s -color cuts and $\Delta\chi^2_{z=2.39}$ criterion in both 53W002 and COSMOS fields.

We selected 60 and 932 objects in the 53W002 and COSMOS fields, respectively. Out of the selected galaxies, 59 and 923 objects are selected also by the original selection where the nebular emission was not included in the model templates. Therefore more than 90% of galaxies are selected regardless of the nebular emission in both fields. Figure 14 shows the distributions of the photometric redshift from the COSMOS2015 catalog (hereafter z_{COS}) for the selected galaxies in the COSMOS field. Indeed, the redshift distribution doesn't change significantly before and after considering the nebular emission. While the number of contaminants from foreground/background objects is smaller when including the nebular emission, a small fraction of galaxies with $z_{\text{COS}} \sim 2.4$ are also missed.

A.2. Physical Properties

In this subsection, we investigate the effects of the nebular emission in the model templates on the physical properties estimated by the SED fitting. As in Section 3.3, we carried out the SED fitting fixing the redshift to $z = 2.39$ to estimate the physical properties of the sample galaxies by using the model templates with the nebular emission. Model templates are the same as in Section A.1. We used the original sample, which were selected by the SED fitting without

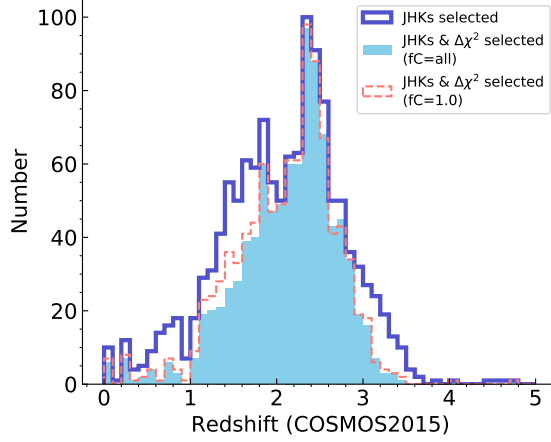


Figure 14. The redshift distribution of the selected objects in the COSMOS field. The photometric redshifts from the COSMOS2015 catalog are used. The blue line histogram shows the distribution for galaxies selected by only the JHK_s -color selection. Light blue shaded histogram shows the result of galaxies selected by the JHK_s -band color and $\Delta\chi^2$ criteria when the nebular emission is included in the model templates used SED fitting, i.e., the $\Delta\chi^2_{z=2.39}$ calculation. Red dashed line histogram shows the distribution of galaxies selected by the original selection where the nebular emission was not included.

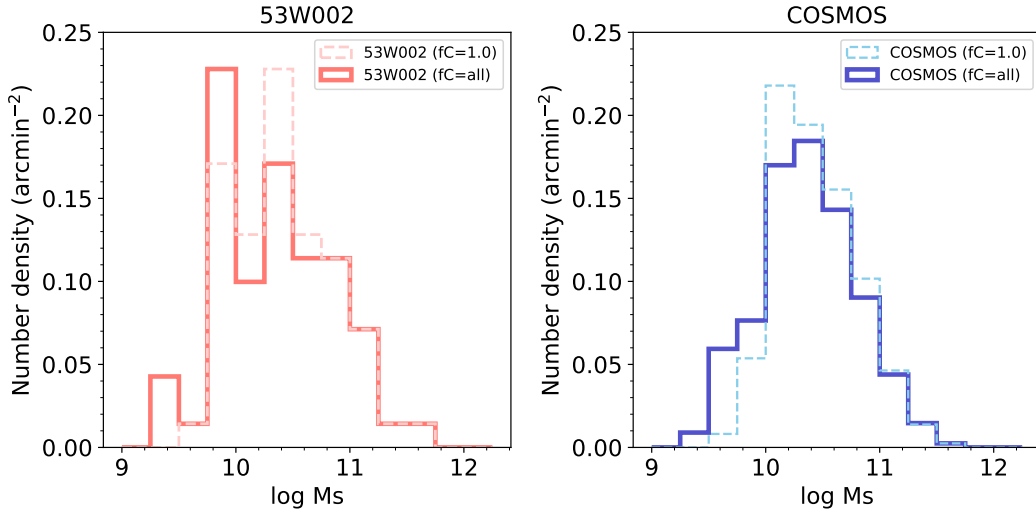


Figure 15. The stellar mass distributions of the JHK_s -selected galaxies in the cases with and without the nebular emission in the SED fitting. The thick solid histogram shows the case with the nebular emission, and the thin dashed histogram represents that without the nebular emission (original analysis).

the nebular emission, in order to compare the estimated physical properties in the case with and without the nebular emission for the same galaxies.

Figure 15 shows the stellar mass distribution of the JHK_s -selected galaxies in the cases with and without the nebular emission in the SED fitting. The stellar mass of relatively massive galaxies with $M_s > 10^{10.5} M_\odot$ is not significantly affected, while that of low-mass galaxies with $M_s < 10^{10.5} M_\odot$ tend to be lower when the nebular emission is included. Lower stellar mass galaxies are more affected by the nebular emission. Figure 16 shows the scatter plot of sSFR vs. M_s , probability density map, and density excess map for the JHK_s -selected galaxies in the case with the nebular emission in the SED fitting. The number and probability density of galaxies with $\text{sSFR} > 10^{-8} \text{ yr}^{-1}$ increase compared to the case where the nebular emission is not included. At $z = 2.39$, strong emission lines of $[\text{OII}]\lambda 3727$, $[\text{OIII}]\lambda\lambda 4959, 5007$, and $\text{H}\alpha$ enter into the J , H , and K_s bands, respectively. These emission lines could affect the broad-band photometry, especially for young star-forming galaxies, where the equivalent widths of these lines tend to be large. Since the

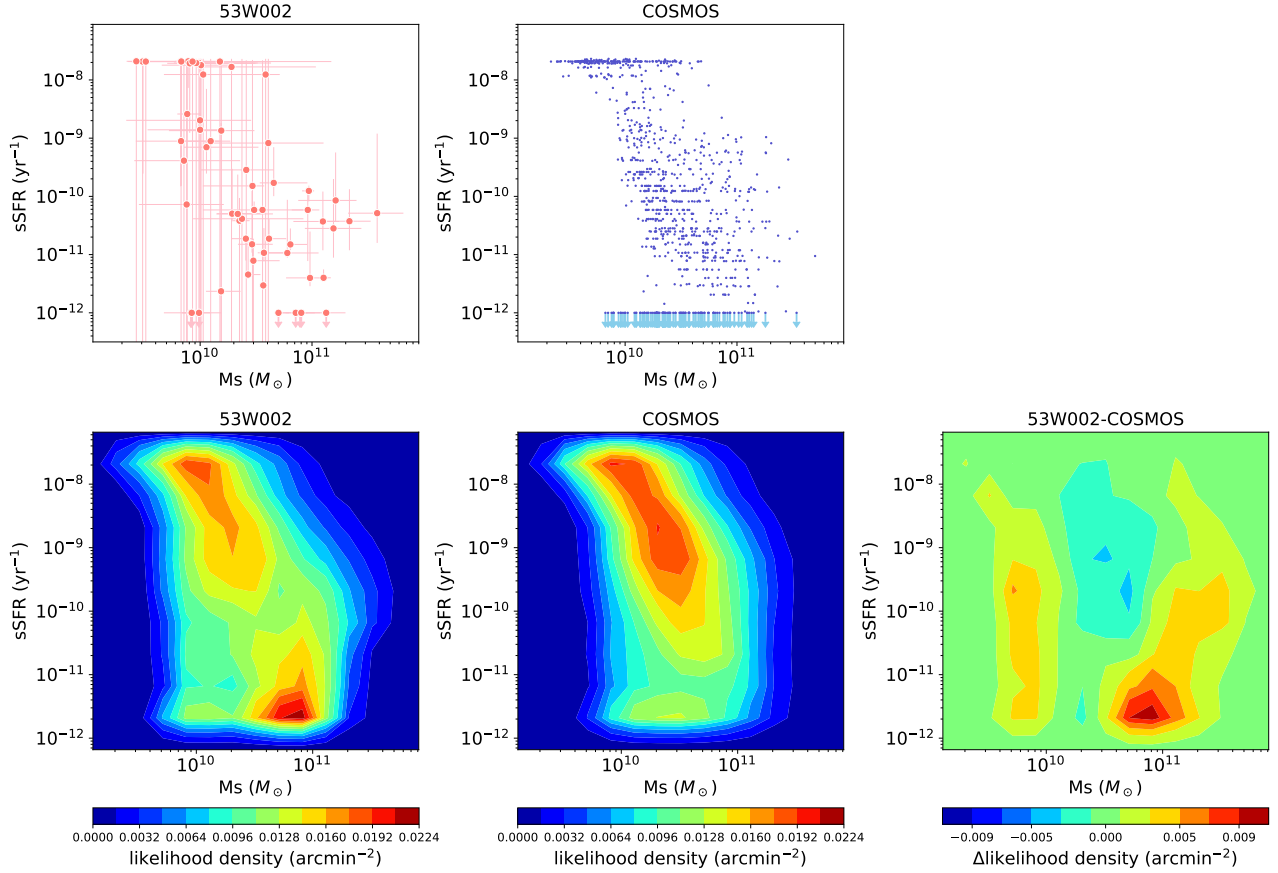


Figure 16. The same as Figure 7, but the nebular emission is included in the SED fitting.

star-forming galaxies at $z \gtrsim 2$ often show strong [OIII] $\lambda\lambda 4959, 5007$ and $H\alpha$ lines relative to the [OII] $\lambda 3727$ line (e.g., Shapley et al. 2015; Steidel et al. 2016), these emission lines could redden $J - K_s$ (and $J - H$) color keeping $H - K_s$ color nearly constant. Such the effects of strong emission lines could mimic that of the Balmer/4000 \AA break in the photometric SED. Indeed, the uncertainty of stellar mass and sSFR for relatively low-mass galaxies becomes larger due to this degeneracy when the nebular emission is included in the fitting (upper panels of Figure 16). Furthermore, a significant fraction of these low-mass galaxies with $M_s \sim 10^{10} M_\odot$ are fitted with very young models with sSFR $\sim 10^{-8} \text{ yr}^{-1}$ in the both fields. Since the strength of this effect seems to be similar in both fields, the probability density excess for low-mass galaxies is not significantly affected by this effect (lower right panel of Figure 16). On the other hand, the effect of the nebular emission do not strongly change the estimation of the physical properties for the massive galaxies probably because of their small equivalent widths of these lines.

Figure 17 is the same as Figure 16, but for mass-weighted age vs. M_s . One can see that a significant fraction of low-mass galaxies show the young ages of $< 10^8 \text{ yr}$ in the both fields. Again, the effect is similar in the both fields, and the probability density excess for low-mass galaxies is not strongly affected. The mass-weighted ages of massive galaxies do not significantly change when the nebular emission is included in the fitting, although there are a few galaxies with younger ages than those in the original analysis at $M_s \sim 10^{10.5} M_\odot$.

Thus the nebular emission could affect the stellar mass, sSFR, and mass-weighted age of low-mass galaxies. We need spectroscopic confirmation of the emission lines and/or the photometric information at longer wavelength to resolve the degeneracy. However, the effects similarly work for those in the 53W002 and comparison field, and therefore the results for low-mass galaxies in this study are not changed so strongly. On the other hand, the estimated physical properties of massive galaxies with $M_s > 10^{10.5} M_\odot$ are not sensitive to the nebular emission unless they have strong emission lines from AGNs.

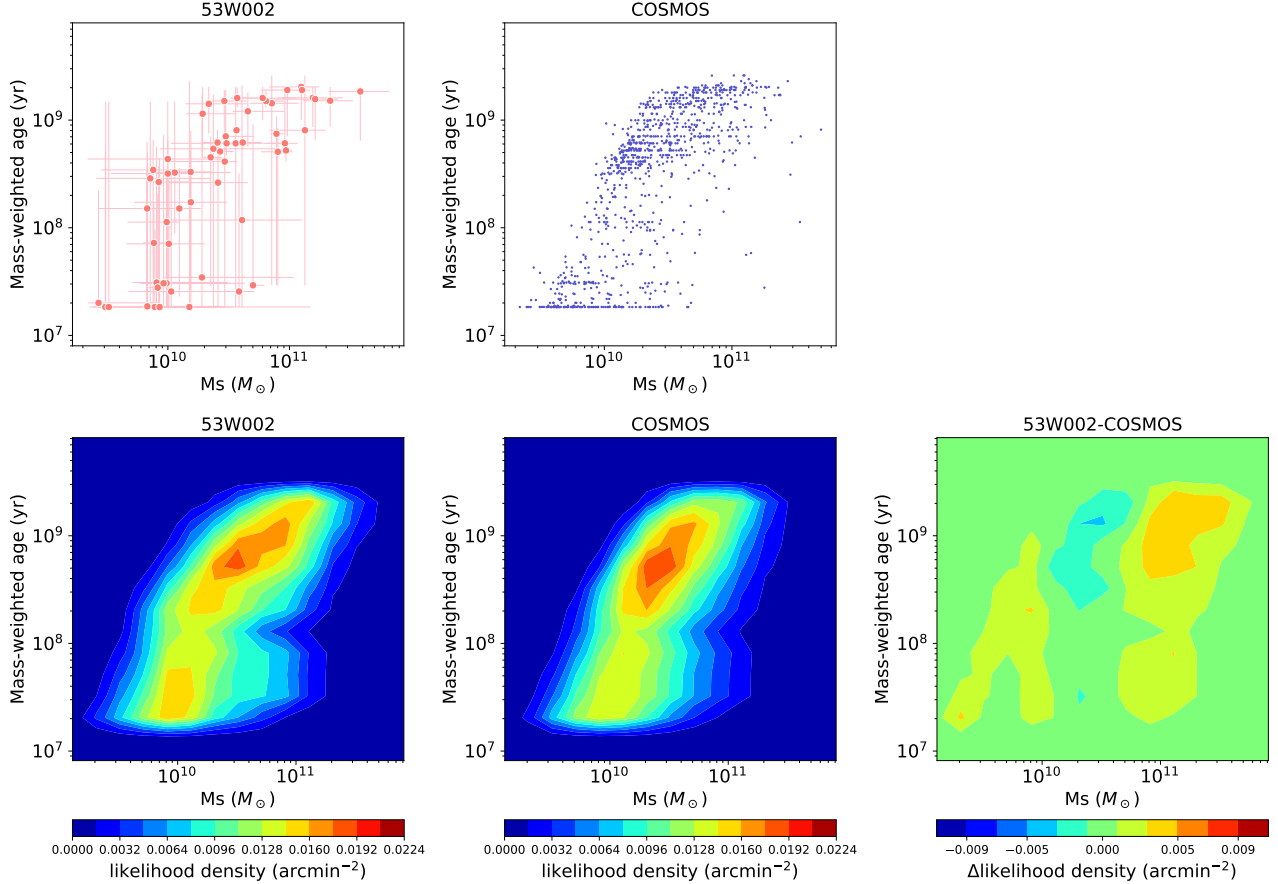


Figure 17. The same as Figure 8, but the nebular emission is included in the SED fitting.

B. EFFECT OF FIXING THE REDSHIFT TO $Z = 2.39$

In Section 4.2, we estimated the physical properties such as M_s , sSFR, and mass-weighted age of the comparison sample fixing their redshifts to $z = 2.39$ in order to subtract the contribution by these field galaxies from the 53W002 data. Since their redshift distribution ranges from $z \sim 1$ to $z \sim 3$, fixing to erroneous redshifts for foreground/background galaxies could systematically affect the distributions of physical properties of these galaxies. For reference, we here present the results of those galaxies with the photometric redshifts from the COSMOS2015 catalog of $z_{COS} = 2.39 \pm 0.20$. Out of 976 galaxies in the comparison sample, 315 galaxies have $z_{COS} = 2.39 \pm 0.20$. In addition to the case of fixing redshift to $z = 2.39$, we performed the same SED fitting analysis fixing redshift to z_{COS} values.

The left and right panels of Figure 18 show the probability density distribution of sSFR vs. M_s estimated by the SED fitting fixing redshift to $z = z_{COS}$ and $z = 2.39$, respectively. We note that the color scale is corrected by multiplying that of Figure 7 by a ratio of the objects numbers of 315/976.

It can be seen from the right panel that the fraction of galaxies with $M_s \sim 10^{10.5} - 10^{11} M_\odot$, in particular, those with $\text{sSFR} = 10^{-11} - 10^{-10} \text{ yr}^{-1}$ increase when we limit the field sample shown in Figure 7 (d) to those at $z = 2.19 - 2.59$. The probability density around $M_s \sim 10^{10} M_\odot$ and $\text{sSFR} \sim 10^{-11} - 10^{-10} \text{ yr}^{-1}$ becomes lower than that in Figure 7 (d). There are probably because the contaminants from foreground/background have relatively low stellar masses when their redshifts are fixed to $z = 2.39$. Except for these difference, the overall distributions are similar with each other. Adopting z_{COS} rather than fixing to $z = 2.39$ does not change the distribution for those with $z_{COS} = 2.39 \pm 0.20$.

The left and middle panels of Figure 19 show the the probability density distribution of mass-weighted age vs. M_s estimated by the SED fitting fixed redshift to $z = z_{COS}$ and $z = 2.39$, respectively. The color scale is also done the correction of the difference of the number count. The field galaxies at $z_{COS} = 2.39 \pm 0.20$ show a higher fraction of those with $M_s \sim 10^{10.5} - 10^{11} M_\odot$ and age $> 10^9 \text{ yr}$ than the all comparison sample. The foreground/background galaxies

tend to show systematically younger ages. As in sSFR vs. M_s plane, result of the probability density distribution of mass-weighted age vs. M_s does not significantly change even if we adopt the photometric redshift of z_{COS} .

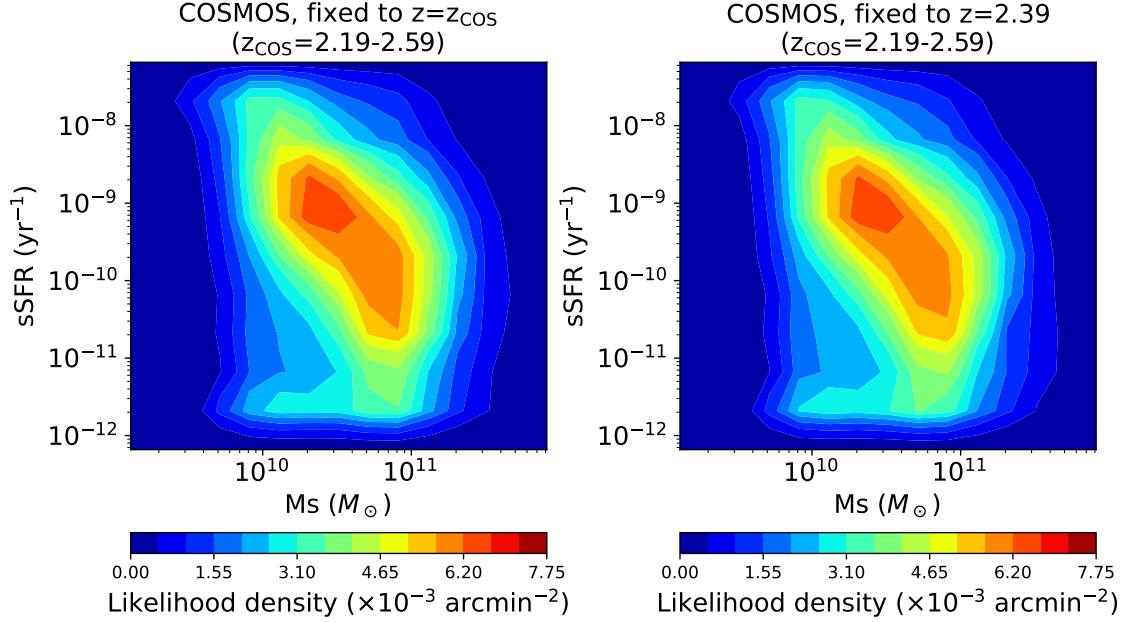


Figure 18. The probability density distributions of the JHK_s -selected galaxies with $z_{\text{COS}} = 2.39 \pm 0.20$ fixing the redshift to $z = z_{\text{COS}}$ (left panel) and $z = 2.39$ (right) for SED fitting when estimating physical properties. The color scale is corrected by multiplying that of Figure 7 by a ratio of object numbers of 315/976.

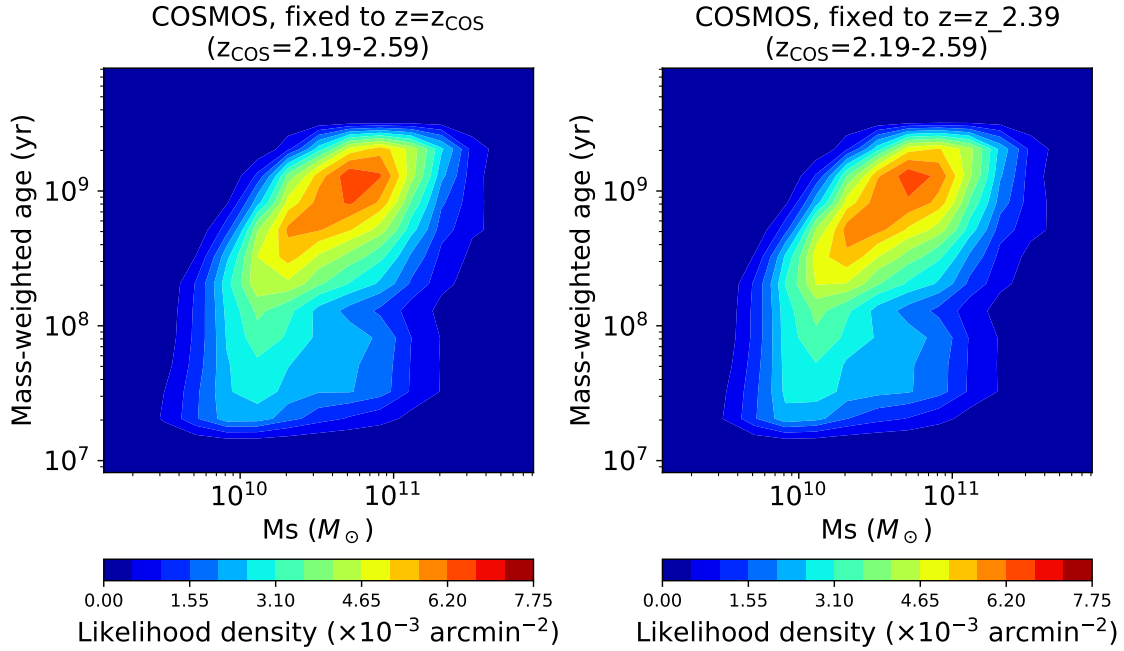


Figure 19. The same as Figure 18, but for mass-weighted age vs. M_s .

REFERENCES

- Ando, M., Shimasaku, K., & Momose, R. 2020, *MNRAS*, 496, 3169
- Aragon-Salamanca, A., Ellis, R. S., Couch, W. J., et al. 1993, *MNRAS*, 262, 764
- Bădescu, T., Yang, Y., Bertoldi, F., et al. 2017, *ApJ*, 845, 172
- Bertin, E. & Arnouts, S. 1996, *A&AS*, 117, 393
- Bower, R. G., Lucey, J. R., & Ellis, R. S. 1992, *MNRAS*, 254, 601
- Bruzual, G. & Charlot, S. 2003, *MNRAS*, 344, 1000
- Calzetti, D., Armus, L., Bohlin, R. C., et al. 2000, *ApJ*, 533, 682
- Chabrier, G. 2003, *PASP*, 115, 763
- Chartab, N., Mobasher, B., Darvish, B., et al. 2020, *ApJ*, 890, 7
- Chiang, Y.-K., Overzier, R., & Gebhardt, K. 2013, *ApJ*, 779, 127
- Cooke, E. A., Hatch, N. A., Muldrew, S. I., et al. 2014, *MNRAS*, 440, 3262
- Cucciati, O., Zamorani, G., Lemaux, B. C., et al. 2014, *A&A*, 570, A16
- Dey, A., Lee, K.-S., Reddy, N., et al. 2016, *ApJ*, 823, 11
- Diener, C., Lilly, S. J., Ledoux, C., et al. 2015, *ApJ*, 802, 31
- Dressler, A. 1980, *ApJ*, 236, 351
- Gawiser, E., Francke, H., Lai, K., et al. 2007, *ApJ*, 671, 278
- Geach, J. E., Sobral, D., Hickox, R. C., et al. 2012, *MNRAS*, 426, 679
- Goto, T., Yamauchi, C., Fujita, Y., et al. 2003, *MNRAS*, 346, 601
- Hagen, A., Ciardullo, R., Gronwall, C., et al. 2014, *ApJ*, 786, 59
- Hatch, N. A., De Breuck, C., Galametz, A., et al. 2011a, *MNRAS*, 410, 1537
- Hatch, N. A., Kurk, J. D., Pentericci, L., et al. 2011b, *MNRAS*, 415, 2993
- Hatch, N. A., Wylezalek, D., Kurk, J. D., et al. 2014, *MNRAS*, 445, 280
- Hayashi, M., Kodama, T., Tadaki, K.-i., et al. 2012, *ApJ*, 757, 15
- Hayashino, T., Matsuda, Y., Tamura, H., et al. 2004, *AJ*, 128, 2073
- Higuchi, R., Ouchi, M., Ono, Y., et al. 2019, *ApJ*, 879, 28
- Husband, K., Bremer, M. N., Stott, J. P., et al. 2016, *MNRAS*, 462, 421
- Ichikawa, T., Suzuki, R., Tokoku, C., et al. 2006, *Proc. SPIE*, 6269, 626916
- Ilbert, O., McCracken, H. J., Le Fèvre, O., et al. 2013, *A&A*, 556, A55
- Inoue, A. K. 2011, *MNRAS*, 415, 2920
- Ito, K., Kashikawa, N., Tanaka, M., et al. 2021, *ApJ*, 916, 35
- Jiang, L., Wu, J., Bian, F., et al. 2018, *Nature Astronomy*, 2, 962
- Kajisawa, M., Kodama, T., Tanaka, I., et al. 2006, *MNRAS*, 371, 577
- Kajisawa, M., Ichikawa, T., Tanaka, I., et al. 2009, *ApJ*, 702, 1393
- Kajisawa, M., Ichikawa, T., Tanaka, I., et al. 2011, *PASJ*, 63, 379
- Keel, W. C., Cohen, S. H., Windhorst, R. A., et al. 1999, *AJ*, 118, 2547
- Khostovan, A. A., Sobral, D., Mobasher, B., et al. 2019, *MNRAS*, 489, 555
- Kodama, T., Tanaka, I., Kajisawa, M., et al. 2007, *MNRAS*, 377, 1717
- Koyama, Y., Polletta, M. del C., Tanaka, I., et al. 2021, *MNRAS*, 503, L1
- Kriek, M., Shapley, A. E., Reddy, N. A., et al. 2015, *ApJS*, 218, 15
- Kuiper, E., Hatch, N. A., Venemans, B. P., et al. 2011, *MNRAS*, 417, 1088
- Kubo, M., Uchimoto, Y. K., Yamada, T., et al. 2013, *ApJ*, 778, 170
- Kubo, M., Yamada, T., Ichikawa, T., et al. 2015, *ApJ*, 799, 38
- Kubo, M., Umehata, H., Matsuda, Y., et al. 2021, *arXiv:2106.10798*
- Kurk, J. D., Röttgering, H. J. A., Pentericci, L., et al. 2000, *A&A*, 358, L1
- Kurk, J. D., Pentericci, L., Röttgering, H. J. A., et al. 2004, *A&A*, 428, 793
- Kusakabe, H., Shimasaku, K., Ouchi, M., et al. 2018, *PASJ*, 70, 4
- Laigle, C., McCracken, H. J., Ilbert, O., et al. 2016, *ApJS*, 224, 24
- Landolt, A. U. 1992, *AJ*, 104, 372
- Lee, K.-S., Dey, A., Cooper, M. C., et al. 2013, *ApJ*, 771, 25
- Lee, K.-S., Dey, A., Hong, S., et al. 2014, *ApJ*, 796, 126
- Lemaux, B. C., Cucciati, O., Tasca, L. A. M., et al. 2014, *A&A*, 572, A41
- Le Fevre, O., Deltorn, J. M., Crampton, D., et al. 1996, *ApJL*, 471, L11
- Leggett, S. K., Currie, M. J., Varricatt, W. P., et al. 2006, *MNRAS*, 373, 781
- Liang, Y., Kashikawa, N., Cai, Z., et al. 2021, *ApJ*, 907, 3
- Lovell, C. C., Thomas, P. A., & Wilkins, S. M. 2018, *MNRAS*, 474, 4612
- Madau, P. 1995, *ApJ*, 441, 18

- Mawatari, K., Yamada, T., Nakamura, Y., et al. 2012, *ApJ*, 759, 133
- Mawatari, K., Inoue, A. K., Yamada, T., et al. 2017, *MNRAS*, 467, 3951
- Mawatari, K., Inoue, A. K., Yamanaka, S., et al. 2020, *Panchromatic Modelling with Next Generation Facilities*, 341, 285
- McCracken, H. J., Milvang-Jensen, B., Dunlop, J., et al. 2012, *A&A*, 544, A156
- Miley, G. K., Overzier, R. A., Tsvetanov, Z. I., et al. 2004, *Nature*, 427, 47
- Miyazaki, S., Komiyama, Y., Sekiguchi, M., et al. 2002, *PASJ*, 54, 833
- Motohara, K., Yamada, T., Iwamuro, F., et al. 2001, *Astrophysical Ages and Times Scales*, 245, 634
- Momose, R., Shimizu, I., Nagamine, K., et al. 2021, *ApJ*, 911, 98
- Momose, R., Shimasaku, K., Nagamine, K., et al. 2021, *ApJL*, 912, L24
- Muldrew, S. I., Hatch, N. A., & Cooke, E. A. 2015, *MNRAS*, 452, 2528
- Muldrew, S. I., Hatch, N. A., & Cooke, E. A. 2018, *MNRAS*, 473, 2335
- Oke, J. B. & Gunn, J. E. 1983, *ApJ*, 266, 713
- Ono, Y., Ouchi, M., Shimasaku, K., et al. 2010, *MNRAS*, 402, 1580
- Ouchi, M., Shimasaku, K., Okamura, S., et al. 2004, *ApJ*, 611, 660
- Ouchi, M., Shimasaku, K., Akiyama, M., et al. 2005, *ApJL*, 620, L1
- Ouchi, M., Shimasaku, K., Furusawa, H., et al. 2010, *ApJ*, 723, 869
- Overzier, R. A., Miley, G. K., Bouwens, R. J., et al. 2006, *ApJ*, 637, 58
- Overzier, R. A., Bouwens, R. J., Cross, N. J. G., et al. 2008, *ApJ*, 673, 143
- Pascarelle, S. M., Windhorst, R. A., Driver, S. P., et al. 1996a, *ApJL*, 456, L21
- Pascarelle, S. M., Windhorst, R. A., Keel, W. C., et al. 1996b, *Nature*, 383, 45
- Pentericci, L., Kurk, J. D., Röttgering, H. J. A., et al. 2000, *A&A*, 361, L25
- Seymour, N., Stern, D., De Breuck, C., et al. 2007, *ApJS*, 171, 353
- Shapley, A. E., Reddy, N. A., Kriek, M., et al. 2015, *ApJ*, 801, 88
- Shi, K., Lee, K.-S., Dey, A., et al. 2019a, *ApJ*, 871, 83
- Shi, K., Huang, Y., Lee, K.-S., et al. 2019b, *ApJ*, 879, 9
- Shi, K., Toshikawa, J., Cai, Z., et al. 2020, *ApJ*, 899, 79
- Shi, K., Toshikawa, J., Lee, K.-S., et al. 2021, *ApJ*, 911, 46
- Shimakawa, R., Kodama, T., Shibuya, T., et al. 2017a, *MNRAS*, 468, 1123
- Shimakawa, R., Kodama, T., Hayashi, M., et al. 2017b, *MNRAS*, 468, L21
- Shimakawa, R., Koyama, Y., Röttgering, H. J. A., et al. 2018, *MNRAS*, 481, 5630
- Shimasaku, K., Ouchi, M., Okamura, S., et al. 2003, *ApJL*, 586, L111
- Snyder, G. F., Brodwin, M., Mancone, C. M., et al. 2012, *ApJ*, 756, 114
- Stanford, S. A., Eisenhardt, P. R., & Dickinson, M. 1998, *ApJ*, 492, 461
- Steidel, C. C., Adelberger, K. L., Dickinson, M., et al. 1998, *ApJ*, 492, 428
- Steidel, C. C., Adelberger, K. L., Shapley, A. E., et al. 2000, *ApJ*, 532, 170
- Steidel, C. C., Adelberger, K. L., Shapley, A. E., et al. 2005, *ApJ*, 626, 44
- Steidel, C. C., Strom, A. L., Pettini, M., et al. 2016, *ApJ*, 826, 159
- Suzuki, R., Tokoku, C., Ichikawa, T., et al. 2008, *PASJ*, 60, 1347
- Tanaka, M., De Breuck, C., Venemans, B., et al. 2010, *A&A*, 518, A18
- Tanaka, I., De Breuck, C., Kurk, J. D., et al. 2011, *PASJ*, 63, 415
- Taniguchi, Y., Scoville, N., Murayama, T., et al. 2007, *ApJS*, 172, 9
- Thomas, R., Le Fèvre, O., Le Brun, V., et al. 2017, *A&A*, 597, A88
- Toshikawa, J., Kashikawa, N., Ota, K., et al. 2012, *ApJ*, 750, 137
- Toshikawa, J., Kashikawa, N., Overzier, R., et al. 2016, *ApJ*, 826, 114
- Toshikawa, J., Uchiyama, H., Kashikawa, N., et al. 2018, *PASJ*, 70, S12
- Uchimoto, Y. K., Yamada, T., Kajisawa, M., et al. 2012, *ApJ*, 750, 116
- Venemans, B. P., Kurk, J. D., Miley, G. K., et al. 2002, *ApJL*, 569, L11
- Venemans, B. P., Röttgering, H. J. A., Overzier, R. A., et al. 2004, *A&A*, 424, L17
- Venemans, B. P., Röttgering, H. J. A., Miley, G. K., et al. 2005, *A&A*, 431, 793
- Venemans, B. P., Röttgering, H. J. A., Miley, G. K., et al. 2007, *A&A*, 461, 823
- Willis, J. P., Canning, R. E. A., Noordeh, E. S., et al. 2020, *Nature*, 577, 39
- Yagi, M., Kashikawa, N., Sekiguchi, M., et al. 2002, *AJ*, 123, 66

Yamada, T., Motohara, K., Iwamuro, F., et al. 2001, PASJ,
53, 1119

Yamada, T., Matsuda, Y., Kousai, K., et al. 2012, ApJ,
751, 29
Yang, Y., Zabludoff, A., Eisenstein, D., et al. 2010, ApJ,
719, 1654